PHYSICAL REVIEW C VOLUME 40, NUMBER 1 JULY 1989

Complex fragments emitted in particle-stable states for the $^{32}S+^{nat}Ag$ reaction at $E/A=22.3$ MeV

H. M. Xu, W. G. Lynch, C. K. Gelbke, M. B. Tsang, D. J. Fields,* M. R. Maier,
D. J. Morrissey, T. K. Nayak, and J. Pochodzalla†
Department of Physics and Astronomy, Department of Chemistry, and National Superconducting Cyclotron Laboratory, Michigan State University, East Lansing, Michigan 48824

D. G. Sarantites and L. G. Sobotka
Department of Chemistry, Washington University, St. Louis, Missouri 63130

M. L. Halbert and D. C. Hensley
Physics Division, Oak Ridge National Laboratory, Oak Ridge, Tennessee 37830
(Received 3 March 1989)

The emission of complex fragments was studied for ^{32}S-induced reactions on ^{nat}Ag at $E/A=22.3$ MeV for angles back of the grazing angle, $\theta_{IMF}=20°$–$50°$. The measured fragment kinetic energy spectra peak at energies near the exit channel Coulomb barriers and decrease exponentially at higher energies. The angular distributions are forward peaked, indicating emission prior to the attainment of full statistical equilibrium of the composite system. The relative populations of a large number of particle stable states of these fragments were measured with a spin spectrometer. Comparisons with statistical calculations which include feeding from known discrete particle unbound states and high-lying continuum states indicate emission temperatures of about 3–4 MeV.

I. INTRODUCTION

The emission of low-energy intermediate mass fragments (IMF), $3 \le Z_f \le 20$, in processes distinct from fission has been observed for a large variety of nuclear reactions.[1–27] In general, the energy spectra of these fragments exhibit broad maxima at energies close to the exit channel Coulomb barrier and exponential slopes at higher energies. The fragment distributions follow[1,7–9,13,20,21,25,27] an approximate power-law dependence on fragment mass $A^{-\tau}$ in both proton and heavy-ion-induced reactions, possibly indicating that the mass distributions are determined by a common physical process. For reactions at intermediate energies, $E/A \approx 20$–500 MeV, the angular distributions are forward peaked indicating that appreciable emission occurs prior to the attainment of statistical equilibrium of the composite projectile-target system (Refs. 6, 11, 13, 15, 16, 18, 20–26, and 28–36). At backward angles, the angular distributions, particularly for heavier fragments, become more isotopic, consistent with significant contributions from the statistical emission by equilibrated heavy reaction residues that could, for example, be formed in incomplete fusion reactions.[14,17,23]

At present, there is no consensus concerning the origin of these fragments. Fragment production has been calculated within statistical,[7–9,16,37–50] as well as purely dynamical,[51–56] models. Most models reproduce selected observables such as the fragment mass distribution. Differences between the various fragmentation models reflect, to a great extent, differences in assumptions concerning the densities, internal excitation, and degree of thermalization which prevail during the later stages of the reaction when the system proceeds from breakup to thermal freezeout. Since the fragment kinetic-energy spectra are sensitive to collective motion, the temporal evolution of the reaction, as well as Fermi motion and Coulomb barrier fluctuations, they do not provide quantitative information concerning the internal excitation energy during the breakup and freezeout stage of the reaction.[16,43,46,47,57–59] Information about the intrinsic excitation and the degree of thermalization at freezeout may be better obtained from the relative populations of nuclear states of the emitted fragments.[28–36,50,60–65]

Emission temperatures of $T \approx 4$–5 MeV were extracted from pairs of widely separated ($\Delta E > T$) particle unbound states in ^4He, ^5Li, and ^8Be at angles significantly greater than the grazing angle where contributions from projectile fragmentation are negligible.[29,30,32–36] The relative populations of these states were found to be surprisingly insensitive to the incident energy over the range of $E/A=35$–94 MeV.[34,35] Moreover, these measurements revealed little sensitivity to the gates placed upon the linear momentum transfer to the target residue[33] or the associated multiplicity of charged particles emitted at forward angles.[36] Slightly lower values, $T \approx 3$ MeV, were extracted[64] from the neutron decays of excited states of ^8Li emitted in the $^{14}N+^{nat}Ag$ reaction at $E/A=35$ MeV. In contrast, significantly lower values, $T \approx 1$ MeV, were extracted[65] from the neutron decays of excited ^{13}C nuclei emitted close to the grazing angle in the $^{14}N+^{165}Ho$ reaction at $E/A=35$ MeV. Finally, measurements involving the γ-ray decays of both low-lying[31,60–62] and high-lying[50,63] particle stable states have been performed. These measurements, particularly those of low-lying states, were more difficult to interpret due to sequential feeding from higher-lying particle unbound states.[28,31,48–50,63]

If the populations of states could be described in terms of thermal equilibrium distributions corresponding to a single emission temperature, this temperature could be unambiguously determined by measuring the relative populations of just two states. On the other hand, the degree of thermalization and the internal consistency of thermal assumptions can only be investigated by measuring a large number of states. Unfortunately, all previous temperature measurements using relative populations of excited states[28–36,50,60–65] were based on only a few states and the degree of thermalization as well as the thermal assumptions could not be addressed. To provide such a test, we have measured the γ-ray decays of a large number of high-lying particle stable states of intermediate mass fragments for ^{32}S-induced reactions on ^{nat}Ag at the incident energy of $E/A=22.3$ MeV. These measurements were performed at angles back of the grazing angle to avoid large contributions from peripheral processes. Previous particle correlation experiments performed[21] for this reaction have established that the fragments are emitted with low average multiplicity, $M_{IMF} \leq 1$, for a broad class of violent projectile target collisions representing about 60–70 % of the total reaction cross section. In these reactions, large amounts (200–400 MeV) of energy are converted into intrinsic degrees of freedom, and a significant fraction of intermediate mass fragment emission takes place prior to the attainment of statistical equilibrium of the composite system.[21]

The rest of this paper is organized as follows. In Sec. II, experimental details will be given. In Sec. III, the inclusive fragment cross sections are presented and fitted with simple parametrizations. The bulk of the particle γ-ray coincidence data are presented in Sec. IV. Calculations for the decay of excited primary fragments are discussed in Sec. V and emission temperatures are extracted in Sec. VI. The paper is summarized and conclusions are drawn in Sec. VII. Details of the γ-ray calibrations are discussed in the Appendices. Some results obtained in this experiment were published previously.[31]

II. EXPERIMENTAL DETAILS

The experiment was performed at the Holifield Heavy Ion Research Facility of Oak Ridge National Laboratory. Silver targets of natural isotopic abundance were irradiated with ^{32}S ions of 714-MeV energy. Intermediate mass fragments were isotopically identified with five ΔE-ΔE-E surface-barrier detector telescopes, positioned at the laboratory angles of $\theta_{IMF}=20°$, 25°, 30°, 45°, and 50°. The telescopes subtended solid angles of $\Delta\Omega=9.8$, 10.1, 15.4, 36.3, and 28.6 msr, respectively. Each telescope consisted of two planar ΔE detectors with thicknesses between 50 and 100 μm and an E detector with thickness of 1.5 mm. Cross contaminations between adjacent isotopes were reduced by restricting the analysis to fragments that stopped in the E detectors of the telescopes thus permitting two independent particle identification gates. This introduced energy thresholds at about $E/A=8$ MeV for ^{10}B at $\theta_{IMF}=20°$, 25°, and 30° and at about $E/A=7$ MeV for $\theta_{IMF}=45°$ and 50°. In order to reduce computer dead time and speed up data acquisition, a hardware gate was set during the experiment which suppressed triggers of the telescopes generated by light particles ($p,d,\ldots,\alpha$). These particles are emitted with significantly larger cross sections than intermediate mass fragments which were the focus of the present experiment. In order to make sure that no nuclei with $Z \geq 3$ were rejected, the gates were set such that a small fraction of α particles were recorded on tape. About 85% of all light particles were rejected by this method.

Coincident γ rays were detected with the spin spectrometer.[66] Six of the NaI(Tl) crystals of the spin spectrometer were replaced by Compton shielded Germanium detector modules. The data obtained with these Germanium detectors have been published in Ref. 31. In addition to the particle γ-ray coincidence events, the spin spectrometer was triggered by the detection in one Germanium detector of 0.898- or 1.836-MeV γ rays from an ^{88}Y source positioned close to the Ag target. With a high probability, a 0.898- (1.836-) MeV γ ray detected in the Germanium ensures the interaction of the companion 1.836- (0.898-) MeV γ ray elsewhere in the spin spectrometer. Using this additional source data, it was possible to monitor the gain shifts of the photomultipliers of NaI(Tl) detectors and make corrections for these gain shifts, run by run, in the off-line analysis.

In the backward hemisphere of the spin spectrometer, neutrons could be suppressed by time-of-flight discrimination. The time-of-flight separation of neutrons from γ rays for detectors in the forward hemisphere of the spin spectrometer was considerably worse due to the large cross sections for fast, noncompound neutrons at forward

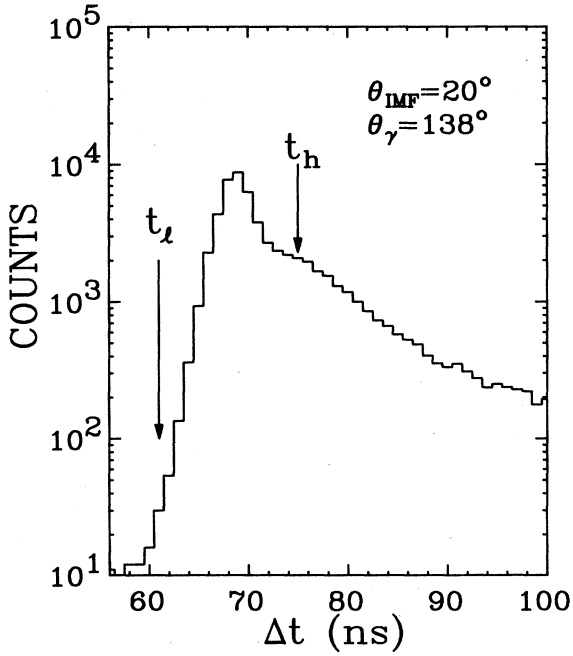

FIG. 1. Relative time spectrum between a particle detector (at $\theta_{IMF}=20°$) and a NaI(Tl) γ-ray detector (at $\theta_\gamma=138°$). The limits of the time gate used for the analysis is indicated by the arrows marked as t_l and t_h.

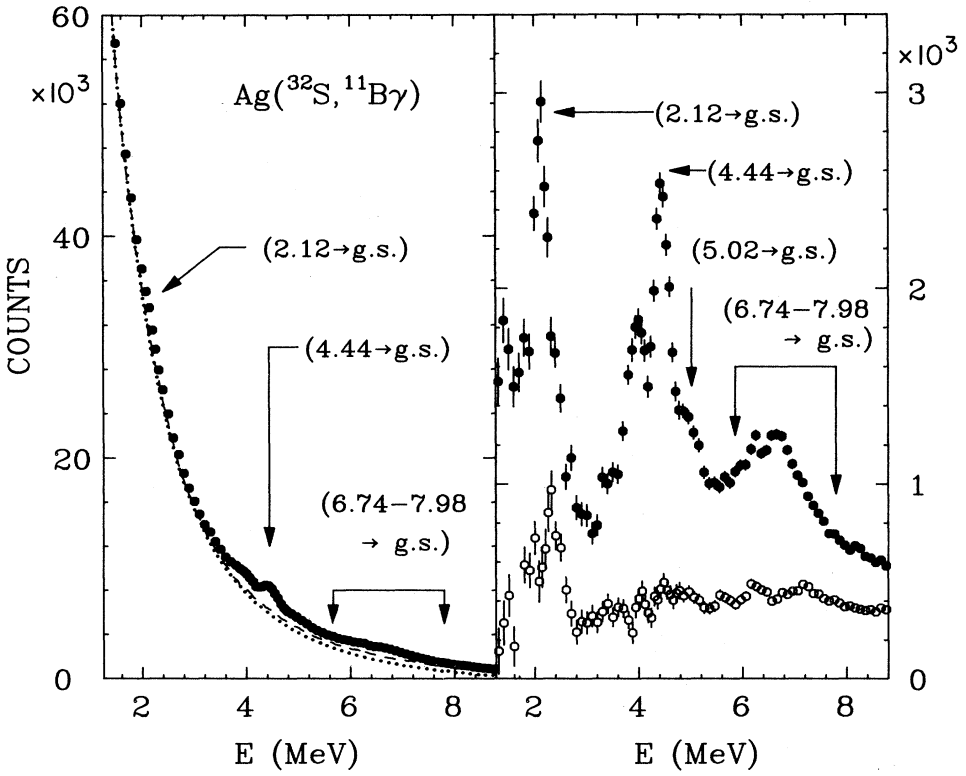

FIG. 2. Left-hand panel: Coincidence (solid circles) and background (dashed line) spectra for ^{11}B fragments. The dotted line corresponds to the function of Eq. (1). Right-hand panel: Coincidence (solid circles) and background (open circles) spectra after subtraction of the function of Eq. (1). The locations of specific γ-ray transitions in ^{11}B are marked by arrows.

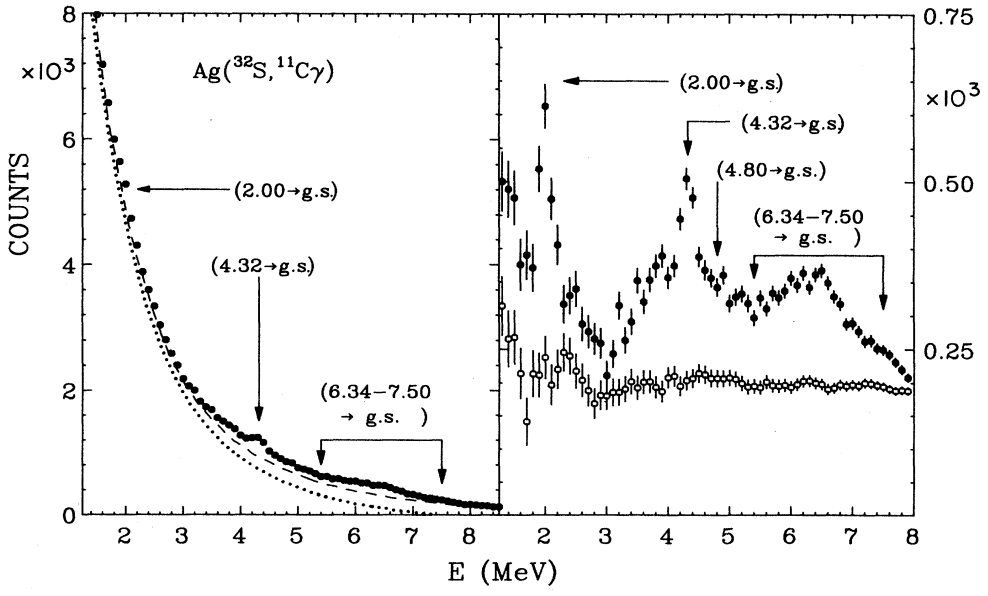

FIG. 3. Left-hand panel: Coincidence (solid circles) and background (dashed line) spectra for ^{11}C fragments. The dotted line corresponds to the function of Eq. (1). Right-hand panel: Coincidence (solid circles) and background (open circles) spectra after subtraction of the function of Eq. (1). The locations of specific γ-ray transitions in ^{11}C are marked by arrows.

angles. To reduce the systematic errors arising from background subtraction, we consequently restricted our analysis to data taken with the NaI(Tl) modules in the backward hemisphere ($\theta_\gamma \geq 90°$) of the spin spectrometer. To illustrate neutron suppression in the backward hemisphere, we show in Fig. 1 the relative time spectrum obtained between a solid-state particle telescope located at $\theta_{IMF}=20°$ and a NaI(Tl) γ-ray detector located at $\theta_\gamma=138°$. The time spectrum clearly exhibits a sharp peak due to prompt γ rays and a long tail caused predominantly by low-energy neutrons emitted from excited target residues. Significant background reductions could be achieved by selecting prompt γ rays with a narrow time gate. The lower and upper limits of the time gate employed for this particular detector pair are shown by the arrows marked as t_l and t_h, respectively.

The energy spectra of coincident γ rays were transformed, event by event, into the rest frames of the detected fragments using relativistic Jacobians and Doppler shift correlations. Since these transformations shift and broaden γ-ray transitions of the target residues, particular attention was paid to identifying and correcting for such effects. For this purpose, background spectra were generated by performing similar transformations to γ-ray spectra measured in coincidence with ^{9}Be nuclei which have no strong transitions at the γ-ray energies of interest. The background spectra were then used in the fitting procedure to extract the yields of γ rays from the decay of the detected intermediate mass fragments.

For illustration, the transformed γ-ray spectra measured in coincidence with ^{11}B, ^{11}C, and ^{12}C fragments are shown in the left-hand panels of Fig. 2–4, respectively. The spectra were summed over all measured particle emission angles and energies and over all γ-ray detectors located in the backward hemisphere. The dashed lines show the corresponding background spectra. On this scale, individual transition are barely, if at all, visible. A better visual comparison of coincidence and background spectra is possible when smooth analytical functions are subtracted from both of them. The dotted curves correspond to functions of the form

$$f(E_\gamma)=A\exp(-E_\gamma/\alpha)+B\exp(-E_\gamma/\beta)+C\ , \qquad (1)$$

where A,B,α,β are constants adjusted by fitting the background and C is a constant offset. The solid and open circles in the right-hand panels show the coincidence and background spectra after subtraction of these functions. On these scales, the individual γ-ray transitions are clearly discernible. Moreover, *spurious* structures of the experimental background spectra are small in comparison with the identified peaks of the coincidence spectra. [The subtraction of the function $f(E_\gamma)$ cancels in the final data reduction; this intermediate step only facilitates a detailed comparison of the coincidence and background spectra in regions of high background.]

The yields of γ rays from the decay of the detected intermediate mass fragment were fitted by folding the detector response function with the energies of known transitions of the detected fragment and adjusting the strengths of the individual transitions and the normalization of the background spectrum. The detector response function was calibrated over the energy range of $E_\gamma \approx 0.5$–7 MeV with γ rays emitted from ^{24}Na, ^{60}Co, ^{88}Y, and ^{207}Bi radioactive sources as well as γ rays produced by the inelastic scattering of protons from ^{12}C and ^{16}O target nuclei. The response function includes detailed descriptions of the photopeak, first, and second escape peaks, as well as line-shape corrections due to coin-

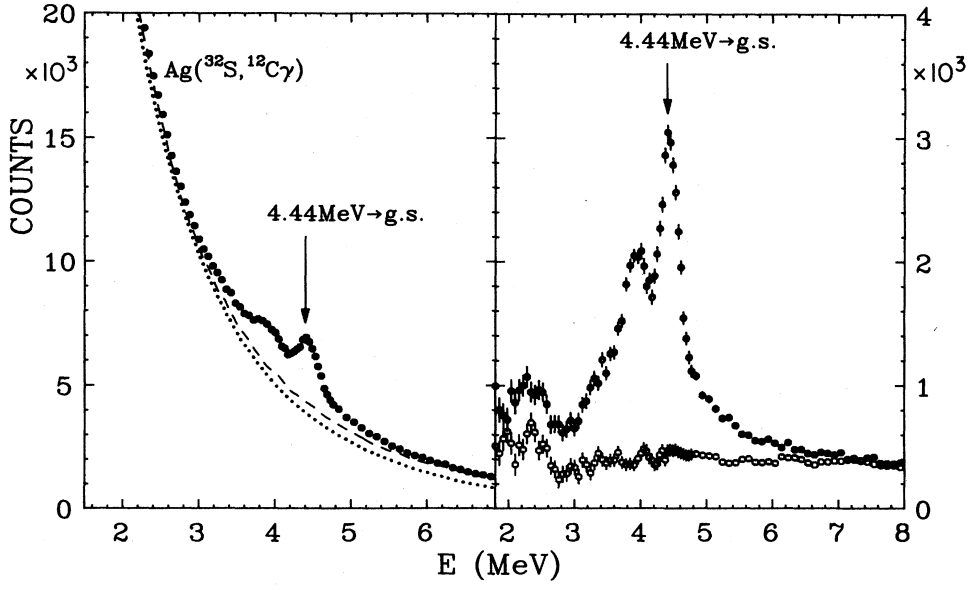

FIG. 4. Left-hand panel: Coincidence (solid circles) and background (dashed line) spectra for ^{12}C fragments. The dotted line corresponds to the function of Eq. (1). Right-hand panel: Coincidence (solid circles) and background (open circles) spectra after subtraction of the function of Eq. (1). The locations of specific γ-ray transitions in ^{12}C are marked by arrows.

cidence summing. Details of the calibrations of the response functions are given in the Appendix. Finally, the inclusive fragment yields and the fragment γ-ray coincidence yields were summed over angle to extract the fraction F_γ of observed fragments which were accompanied by the designated γ ray.

The effects of coincidence summing are illustrated for the simple case of the 4.44-MeV γ-ray transition of excited ^{12}C fragments (see Fig. 4 for the coincidence and background spectra). The final coincidence yield after background subtraction is shown by the solid circles in Fig. 5. The dashed curve shows the detector responses as calibrated via the $^{12}C(p,p')^{12}C^*_{4.44}$ reaction for which the γ-ray multiplicity is one. This calibration underpredicts the high-energy tail of the line shape for the spectrum measured in the $^{nat}Ag(^{32}S,^{12}C\gamma)$ reaction in which the

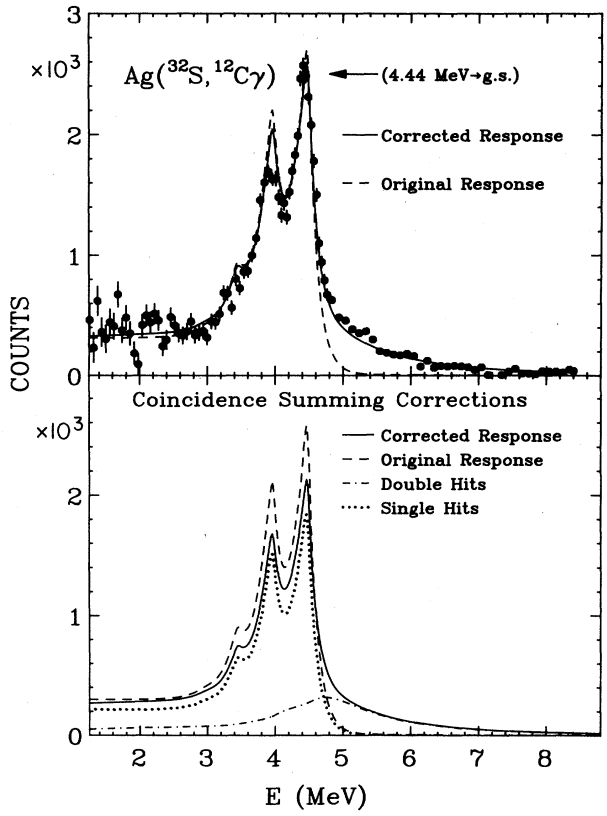

FIG. 5. Upper panel: Background subtracted coincidence yield (solid circles) attributed to γ-ray decays of excited ^{12}C fragments. The location of the photopeak for the decay of the 4.44-MeV states is marked by an arrow. The dashed line shows the original response function determined from the calibration at low γ-ray multiplicity. The solid line shows the final line shape which includes corrections due to coincidence summing. Lower panel: Corrections due to coincidence summing at high γ-ray multiplicity. The solid and dashed lines are the same as in the upper panel. The dashed-dotted curve corresponds to the calculated response due to the simultaneous detection of two γ rays; the dotted line corresponds to the undistorted response when only the 4.44-MeV γ ray is detected. The solid line corresponds to the sum of the dotted and dashed-dotted lines.

average γ-ray multiplicity is high. Due to this high γ-ray multiplicity, there is a nonnegligible probability that two coincident γ rays or a γ ray and a neutron are detected in a single NaI(Tl) module. We denote this effect as "coincidence summing;" it depends on the associated γ-ray and neutron multiplicities and on the geometry of the experiment, but is independent of the beam intensity. The calculation of the line-shape distortion due to coincidence summing is described in the Appendix. The corrections are illustrated in the lower part of Fig. 5. The dashed line shows the response of the detector to a given number of 4.44-MeV γ rays in the absence of coincidence summing. A fraction, p ($\approx$0.28), of these γ rays, will interact with the detector in coincidence with a second γ ray or a neutron from the same reaction. The summed response to the 4.44-MeV γ ray plus the second γ ray or neutron is shown by the dashed-dotted curve. The remaining fraction, $1-p$, of the 4.44-MeV γ rays will interact individually with the detector with the response function measured at low multiplicities and shown by the dotted curve. The total response function, corrected for coincidence summing, is shown by the solid lines in Fig. 5; it corresponds to the sum of the yields represented by the

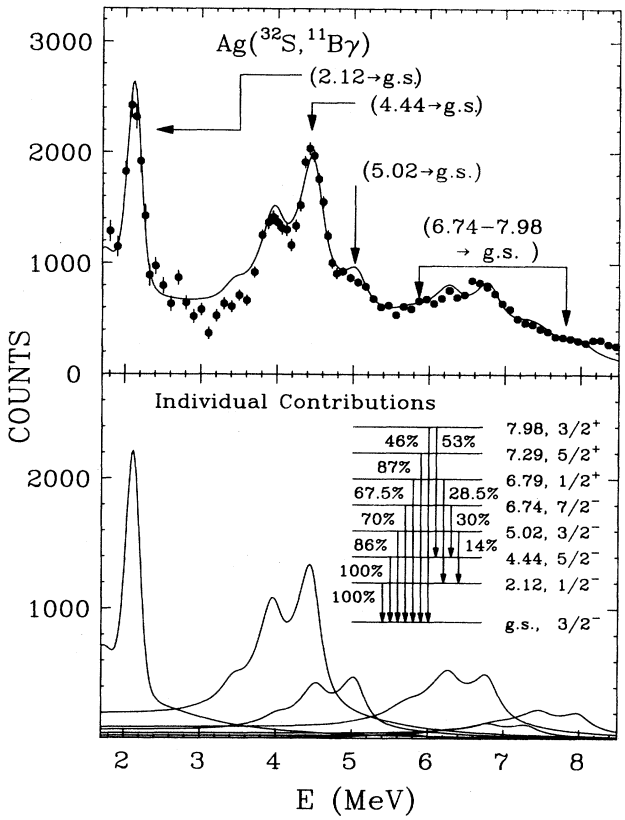

FIG. 6. Upper panel: Background subtracted coincidence yield (solid circles) attributed to γ-ray decays of excited ^{11}B fragments. The solid line shows the fit used for the extraction of the γ-ray fractions, F_γ, listed in Table II. The locations of several strong transitions are shown by arrows. Lower panel: Contributions from individual transitions. Important transitions and branching ratios are given in the inset.

dotted and dashed-dotted curves [see also Eq. (A18) of the Appendix]. This parameter-free correction reproduces the measured coincidence yield rather well. All fitted spectra include corrections due to coincidence summing.

Coincidence summing corrections were also required to extract the γ-ray yields from measurements obtained with the Compton suppressed Germanium detectors of the spin spectrometer. Because of the superior resolution of the Germanium detectors, individual γ-ray hits are well separated from summed events and corrections to the line shape are not required. In the Compton suppressed operating mode, however, additional γ rays or neutrons detected in the Germanium detector or the Compton shield result in a multiplicity dependent loss of efficiency of about 20%. Previous measurements obtained with the Compton suppressed Germanium detectors[31] have now been corrected for this loss of efficiency and are included in Figs. 23 and 24.

Figures 6 and 7 give examples for more complicated coincidence spectra. The solid circles show the final coincidence yields from ^{11}B (Fig. 6) and ^{11}C (Fig. 7) γ decays, after background subtraction. (The original coincidence and background spectra were already shown in Figs. 2 and 3.) The photopeak locations of the most important γ-ray transitions are marked by arrows. The lower panels show individual contributions from the most important transitions used in the fits. The most important transitions and branching ratios used in the final fits are shown in the insets. Clearly, the individual populations of states above about 6 MeV excitation energy are not well determined. In these and other ambiguous cases, we have used the summed strengths of the groups of states indicated in the upper parts of the figures to provide information about the emission temperature.

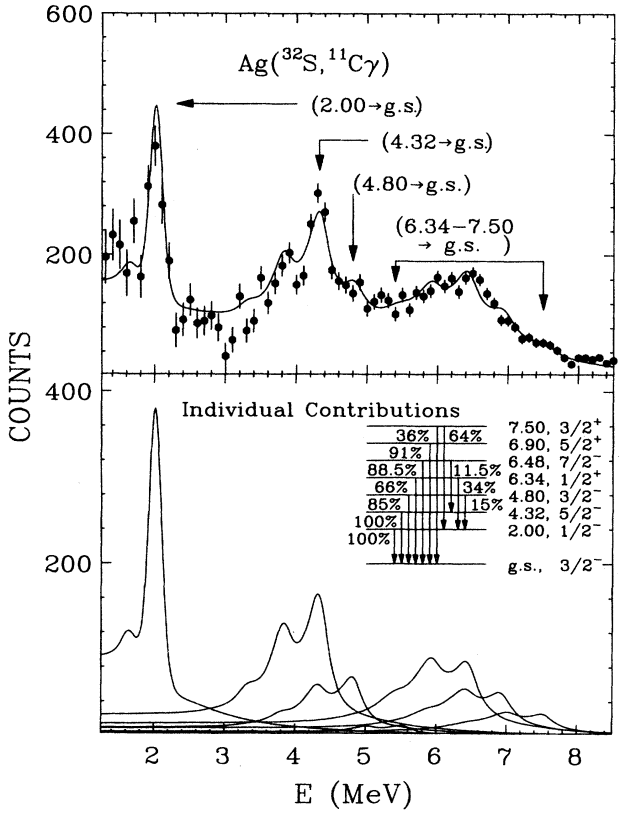

FIG. 7. Upper panel: Background subtracted coincidence yield (solid circles) attributed to γ-ray decays of excited ^{11}C fragments. The solid line shows the fit used for the extraction of the γ-ray fractions F_γ listed in Table II. The locations of several strong transitions are shown by arrows. Lower panel: Contributions from individual transitions. Important transitions and branching ratios are given in the inset.

III. INCLUSIVE FRAGMENT CROSS SECTIONS

The inclusive differential cross sections, measured at $\theta_{IMF}=20°$, 30°, 45°, and 50°, are shown in Figs. 8–12 for isotopes of lithium, beryllium, boron, carbon, nitrogen, and oxygen, respectively. Consistent with previous measurements,[21] the spectra exhibit broad maxima at energies close to the exit channel Coulomb barrier and rather featureless, nearly exponential slopes at higher energies. These slopes become steeper at larger angles. In the center-of-mass system, the cross sections are peaked at forward angles, indicating emission prior to the establishment of full statistical equilibrium of the composite nuclear system. In order to obtain analytical interpolations of the inclusive cross sections to unmeasured angles and

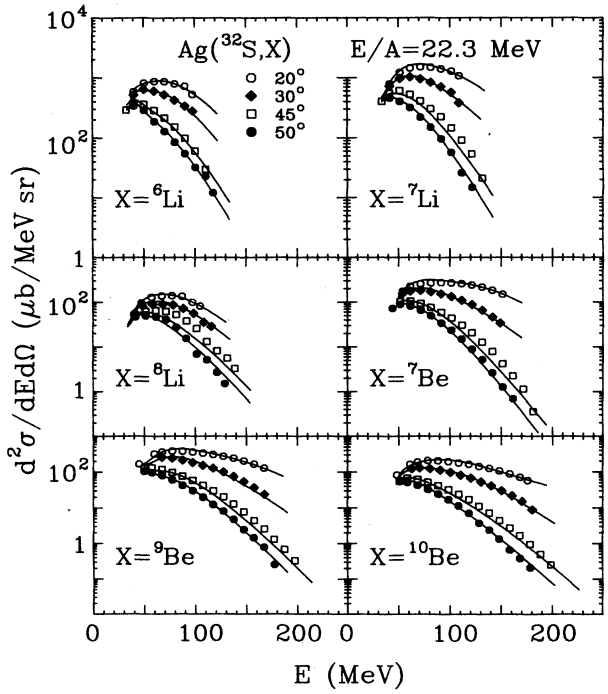

FIG. 8. Inclusive differential cross sections for lithium and beryllium isotopes; the laboratory detection angles are indicated in the figure. The solid lines represent fits with Eq. (2); the parameters are listed in Table I.

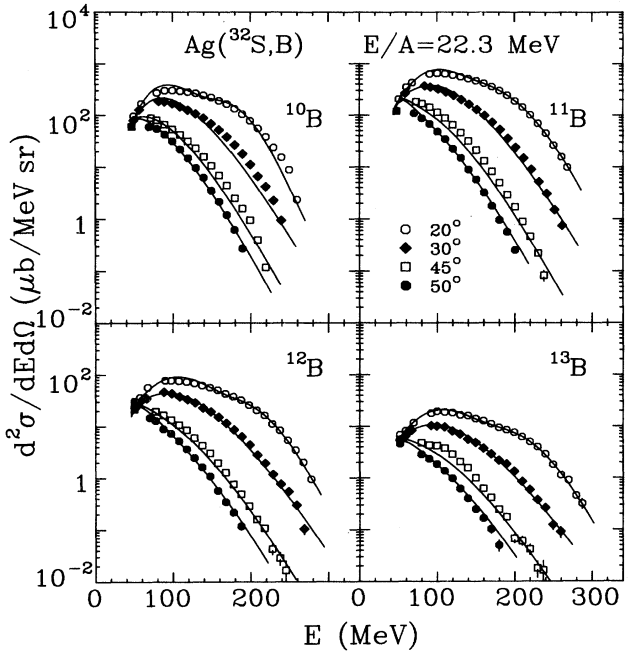

FIG. 9. Inclusive differential cross sections for boron isotopes; the laboratory detection angles are indicated in the figure. The solid lines represent fits with Eq. (2); the parameters are listed in Table I.

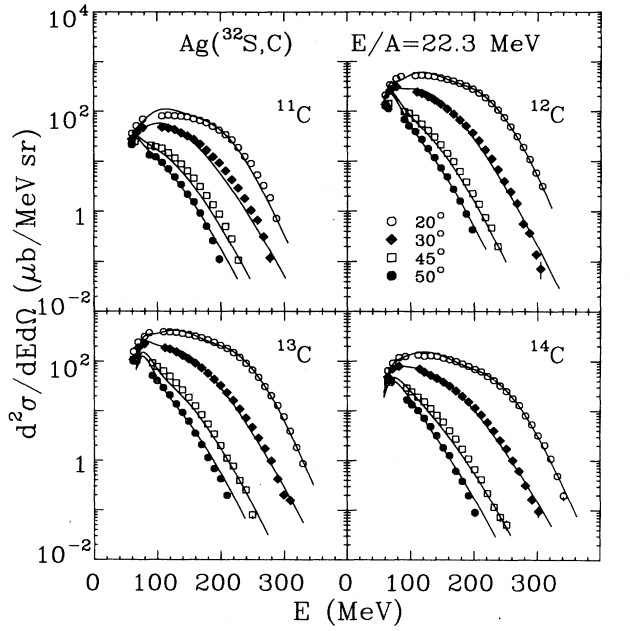

FIG. 10. Inclusive differential cross sections for carbon isotopes; the laboratory detection angles are indicated in the figure. The solid lines represent fits with Eq. (2); the parameters are listed in Table I.

energies, the data were fitted by a parametrization employing the superposition of three Maxwellian distributions ("moving sources")

$$\frac{d^2\sigma}{d\Omega\, dE} = \sum_{i=1}^{3} N_i \sqrt{E-U_c} \times \exp\{-[E-U_c+E_i - 2\sqrt{E_i(E-U_c)}\cos\theta]/T_i\}\ . \tag{2}$$

Here, U_c is the kinetic energy gained by the Coulomb repulsion from the heavy reaction residue assumed to be stationary in the laboratory system, N_i is a normalization constant, and T_i is the "kinetic temperature" parameter of the ith source, $E_i = \frac{1}{2}mv_i^2$, where m is the mass of the emitted particle and v_i is the velocity of the ith source in the laboratory system. This choice of parametrization was chosen for simplicity; it is not unique.[59] Fits obtained with this parametrization are shown by the solid lines in Figs. 8–12; the parameters are listed in Table I. Because of the small angular range covered by the data, substantial ambiguities exist for the individual parameters.

IV. γ-RAY SPECTRA FROM DECAYING FRAGMENTS

The γ-ray spectra detected in coincidence with ^{10}Be, ^{12}B, ^{13}C, ^{14}C, ^{14}N, ^{15}N, ^{16}O, and ^{18}O fragments are shown in the left-hand panels of Figs. 13–20, respectively. The respective background spectra are represented by the dashed lines. The right-hand panels show the yields obtained after subtraction of the background spectra. These yields are associated with γ-ray transitions in the detected fragments. The solid lines show the fits used for the extraction of the γ-ray fractions, F_γ. The insets in

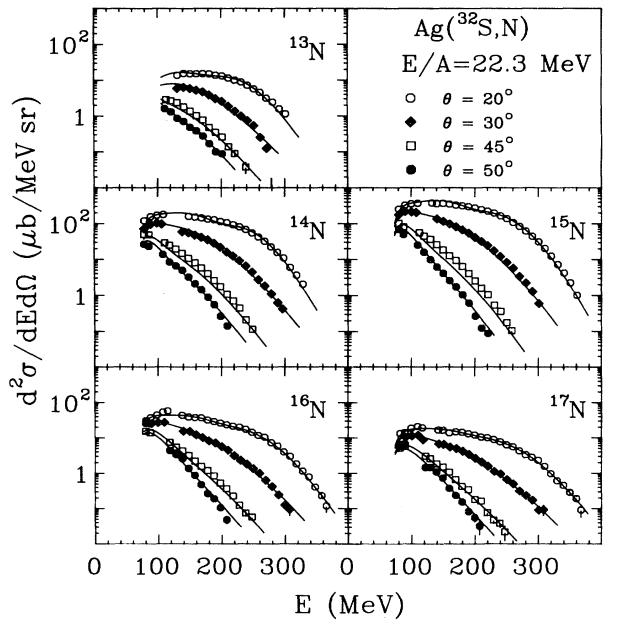

FIG. 11. Inclusive differential cross sections for nitrogen isotopes; the laboratory detection angles are indicated in the figure. The solid lines represent fits with Eq. (2); the parameters are listed in Table I.

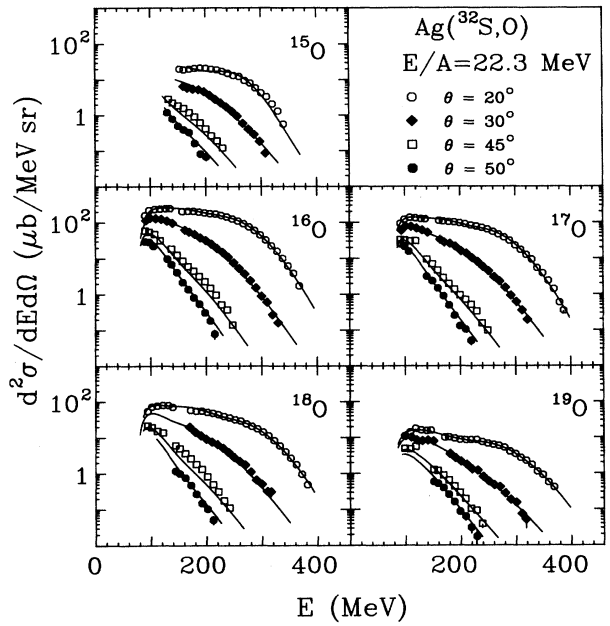

FIG. 12. Inclusive differential cross sections for oxygen isotopes; the laboratory detection angles are indicated in the figure. The solid lines represent fits with Eq. (2); the parameters are listed in Table I.

the left-hand panels show the most important transitions and branching ratios. Photopeak locations of important transitions or groups of transitions are indicated by arrows in the right-hand panels. For the actual fits, we used the complete set of transitions and branching ratios from the compilation of Ref. 67. The γ-ray yields associated with decays of excited ^{11}B, ^{11}C, and ^{12}C transitions were already presented in Figs. 5–7.

For ^{12}C, ^{13}C, and ^{10}B fragments we have investigated whether the measured values of F_γ depend on the fragment kinetic energy or scattering angle. Within the experimental uncertainties, no dependence of the F_γ's on either quantity was observed. Values for F_γ, listed in Table II, were obtained by combining the data for the various intermediate mass fragment kinetic energies and scattering angles.

The coincident γ-ray spectra can be well understood in terms of known transitions in the detected fragments. The good agreement of the measured and fitted spectral shapes justifies, *a posteriori*, our treatment of the background associated with emissions from target residues. The only case which shows noticeable deviations from our standard calibration and background subtraction procedures corresponds to the width of the 0.95-MeV γ-ray peak measured in coincidence with ^{12}B fragments, see Fig. 14. This peak results from the superposition of the decays ^{12}B(2^+,0.953 MeV)$\rightarrow\gamma+^{12}$B(1^+,g.s.) and ^{12}B(1^-,2.621 MeV)$\rightarrow\gamma+^{12}$B(2^-,1.674 MeV). For this low-energy γ ray, the linewidth was somewhat larger than expected from the overall calibration of the response function, suggesting that the resolution of the spin spectrometer was slightly worse during the experiment than during the calibration. This degradation of the resolution could possibly arise from the coincidence summing of low-energy γ rays and x rays which lie below our experimental thresholds and therefore are not taken into account by the coincidence summing corrections described in the Appendix. This resolution problem made the background determination and subsequent subtraction

TABLE I. Parameters used for the fits of the inclusive cross sections with Eq. (2). The temperature parameters T_i are given in units of MeV and the normalization constants N_i are given in units of μb/(sr MeV$^{3/2}$).

Isotope	v_1/c	T_1	N_1	v_2/c	T_2	N_2	v_3/c	T_3	N_3	U_c
^{6}Li	0.156	5.1	73.5	0.095	9.6	219.9	0.025	5.0	226.4	35.0
^{7}Li	0.143	8.6	229.7	0.081	9.6	369.7	0.007	5.0	270.6	34.6
^{8}Li	0.160	5.0	0.1	0.090	11.0	34.3	0.009	13.7	17.1	34.3
^{7}Be	0.161	7.7	65.7	0.085	10.1	73.1	0.018	5.0	41.3	45.4
^{9}Be	0.154	6.8	74.6	0.086	10.0	107.9	0.000	5.0	121.5	44.5
^{10}Be	0.180	5.5	57.7	0.105	10.2	48.9	0.043	10.4	29.7	44.1
^{10}B	0.172	2.5	5675.6	0.097	10.5	92.8	0.001	12.7	42.6	47.0
^{11}B	0.167	4.0	977.7	0.101	10.4	190.3	0.008	11.7	106.8	46.6
^{12}B	0.173	2.7	1494.4	0.102	11.0	21.9	0.014	12.5	12.0	46.3
^{13}B	0.167	3.3	127.4	0.097	12.0	4.8	0.013	13.1	2.3	46.0
^{11}C	0.164	3.5	260.2	0.100	11.2	26.0	0.013	9.0	17.2	58.0
^{12}C	0.165	3.8	1608.1	0.102	10.1	156.9	0.022	8.4	139.0	58.8
^{13}C	0.162	3.5	1787.7	0.100	10.1	107.1	0.037	6.7	98.6	66.8
^{14}C	0.164	3.5	930.5	0.102	10.6	37.5	0.038	10.2	23.7	58.0
^{13}N	0.165	3.6	125.5	0.102	12.3	3.8	0.001	11.4	4.6	69.3
^{14}N	0.169	2.7	11 904.2	0.105	10.5	49.5	0.051	7.4	37.0	68.9
^{15}N	0.164	3.2	8122.8	0.106	9.6	123.1	0.051	8.0	79.0	68.5
^{16}N	0.159	3.8	211.4	0.102	11.4	9.6	0.043	10.4	9.5	68.5
^{17}N	0.155	4.5	40.3	0.104	11.9	3.6	0.048	11.6	3.5	67.8
^{15}O	0.164	2.8	2206.9	0.106	11.6	5.6	0.052	7.5	7.0	76.9
^{16}O	0.159	4.2	1254.1	0.107	9.8	66.3	0.057	7.8	55.9	76.5
^{17}O	0.158	3.8	1254.4	0.107	10.1	33.6	0.054	8.3	32.4	76.1
^{18}O	0.158	4.0	557.1	0.103	10.4	19.8	0.051	8.1	19.5	75.7
^{19}O	0.149	5.5	22.1	0.099	12.6	2.0	0.055	11.8	3.1	75.4

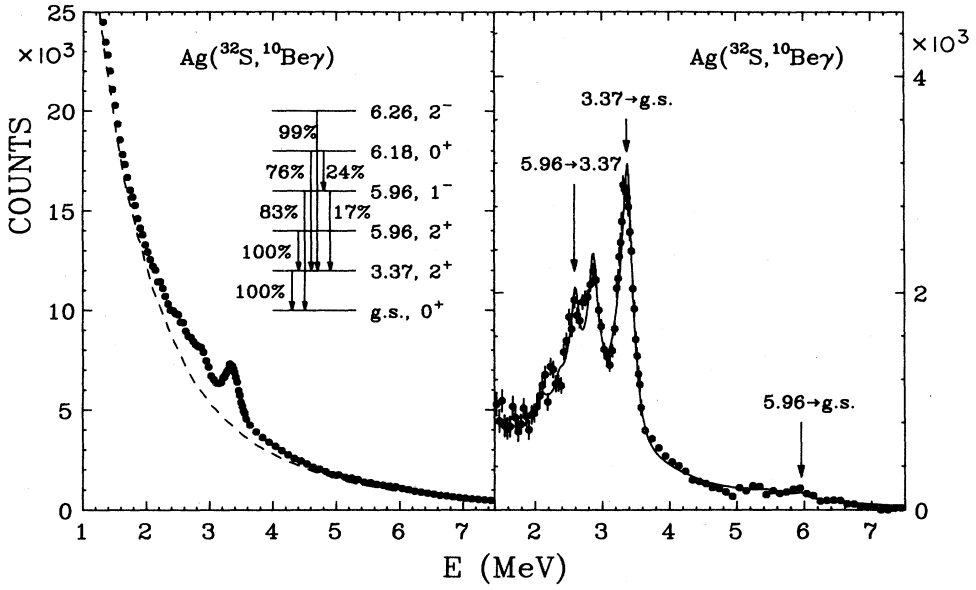

FIG. 13. γ-ray spectra measured in coincidence with ^{10}Be fragments. The left-hand panel shows the raw coincidence spectrum with the background indicated by the dashed line. The right-hand panel shows the spectrum associated with γ-ray decays of excited ^{10}Be fragments. The solid line shows the fit used for the extraction of the γ-ray fractions, F_γ, listed in Table II. The inset shows important transitions and branching ratios used for the fit. Photopeak locations of important transitions are indicated by arrows.

more difficult for γ-ray energies below about 1 MeV. In order to extract the strength of this peak more accurately, the spectrum was fitted by folding the calibrated response function with a Gaussian of 0.14 MeV full width at half maximum (FWHM) (while conserving the integral normalization of the spectrum). The γ-ray fraction extracted from this peak agrees within 10% with that extracted[31] from the γ-ray spectra measured with the Compton shielded Germanium detectors for which the background subtraction was less problematic.

For a considerable number of transitions, the energy resolution of the NaI(Tl) detectors was insufficient to al-

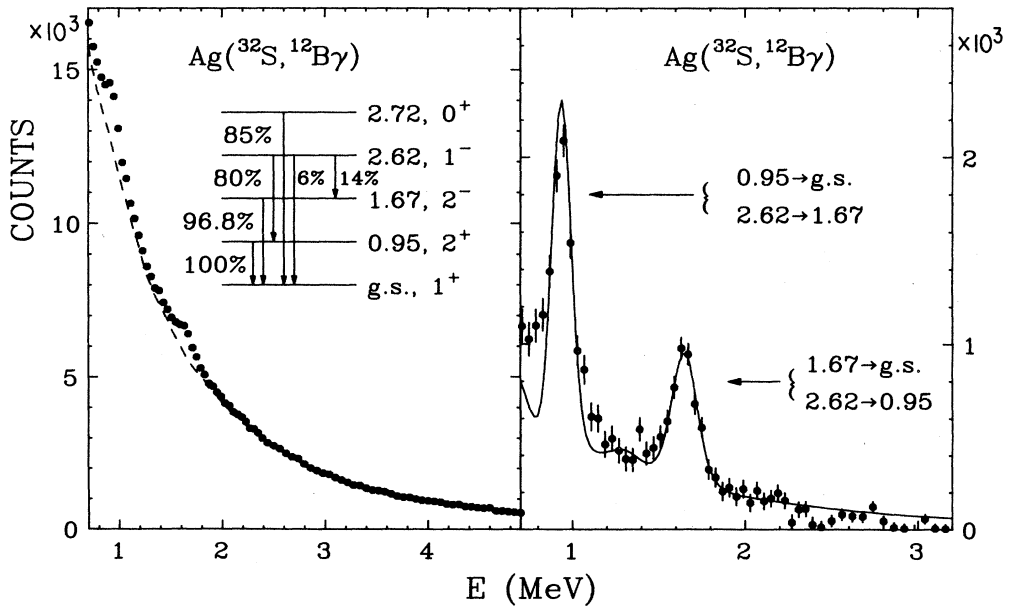

FIG. 14. γ-ray spectra measured in coincidence with ^{12}B fragments. The left-hand panel shows the raw coincidence spectrum with the background indicated by the dashed line. The right-hand panel shows the spectrum associated with γ-ray decays of excited ^{12}B fragments. The solid line shows the fit used for the extraction of the γ-ray fractions, F_γ, listed in Table II. The inset shows important transitions and branching ratios used for the fit. Photopeak locations of important transitions are indicated by arrows.

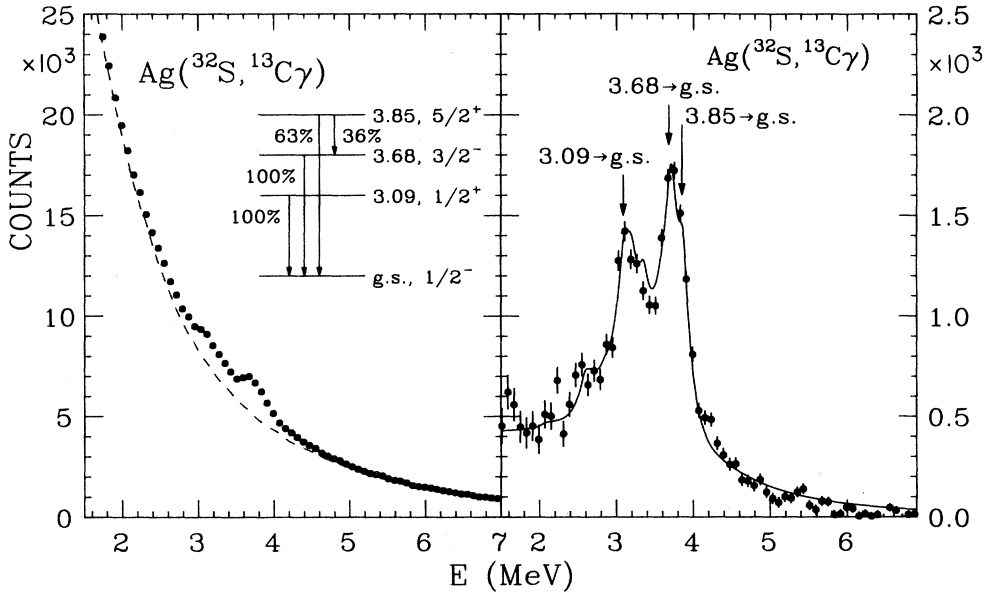

FIG. 15. γ-ray spectra measured in coincidence with ^{13}C fragments. The left-hand panel shows the raw coincidence spectrum with the background indicated by the dashed line. The right-hand panel shows the spectrum associated with γ-ray decays of excited ^{13}C fragments. The solid line shows the fit used for the extraction of the γ-ray fractions, F_γ, listed in Table II. The inset shows important transitions and branching ratios used for the fit. Photopeak locations of important transitions are indicated by arrows.

low reliable determination of the individual γ-ray fractions. In such cases, the γ-ray fractions are only given for groups of transitions which could be determined with good statistical accuracy. Transitions contained within a particular group are identified in Table II by subscripts $\sum 1, \sum 2, \ldots$, etc.

There are several sources for the uncertainties in the γ-ray fractions listed in Table II. Because the resolution for low-energy γ rays could not be accurately assessed from the fragment γ-ray coincidence data, the extracted γ-ray fractions have associated uncertainties which could be as large as 10% for γ-ray energies significantly below

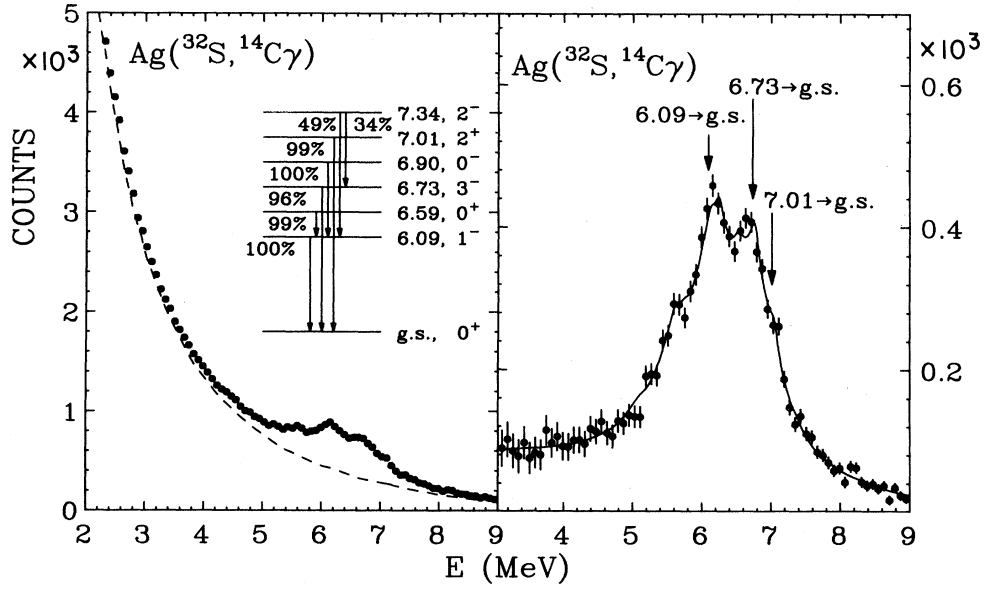

FIG. 16. γ-ray spectra measured in coincidence with ^{14}C fragments. The left-hand panel shows the raw coincidence spectrum with the background indicated by the dashed line. The right-hand panel shows the spectrum associated with γ-ray decays of excited ^{14}C fragments. The solid line shows the fit used for the extraction of the γ-ray fractions, F_γ, listed in Table II. The inset shows important transitions and branching ratios used for the fit. Photopeak locations of important transitions are indicated by arrows.

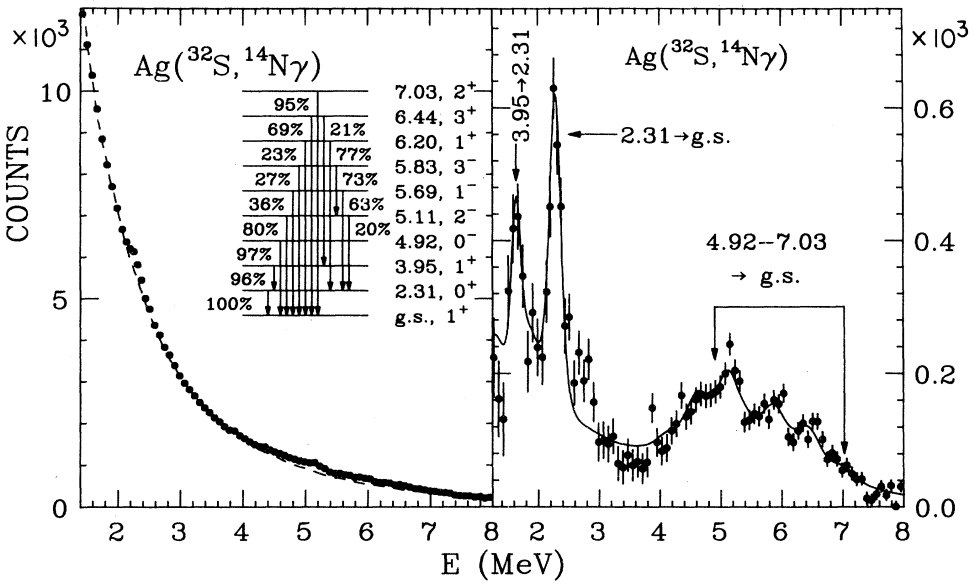

FIG. 17. γ-ray spectra measured in coincidence with ^{14}N fragments. The left-hand panel shows the raw coincidence spectrum with the background indicated by the dashed line. The right-hand panel shows the spectrum associated with γ-ray decays of excited ^{14}N fragments. The solid line shows the fit used for the extraction of the γ-ray fractions, F_γ, listed in Table II. The inset shows important transitions and branching ratios used for the fit. Photopeak locations of important transitions are indicated by arrows.

significantly below 3 MeV. Above 3 MeV these uncertainties are less than 2%. Additional uncertainties are associated with low counting statistics, uncertainties in the interpolation of the γ-ray efficiency (see the Appendix), ambiguities in the fitting procedure, and the possibility for misidentification of the mass and charge of the intermediate mass fragment detected in the particle telescope. These uncertainties were estimated and for simplicity, were combined in quadrature to provide the uncertainties listed in Table II. It was particularly difficult to estimate the uncertainty associated with possible errors in the functional form of the background. Upper limits on this uncertainty were obtained by fitting with different background assumptions. With extreme background assumptions, the experimentally determined yield varied by

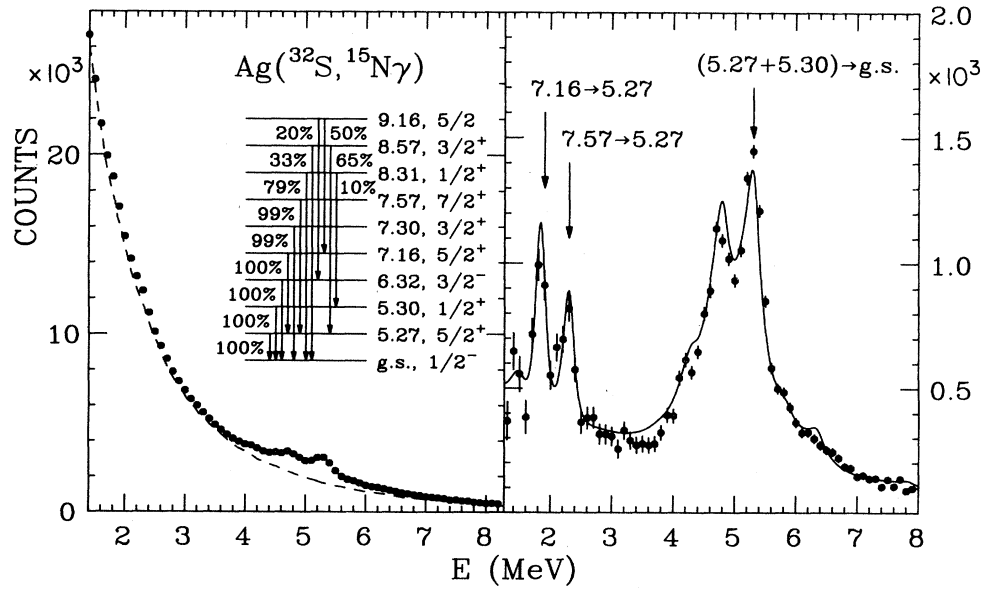

FIG. 18. γ-ray spectra measured in coincidence with ^{15}N fragments. The left-hand panel shows the raw coincidence spectrum with the background indicated by the dashed line. The right-hand panel shows the spectrum associated with γ-ray decays of excited ^{15}N fragments. The solid line shows the fit used for the extraction of the γ-ray fractions, F_γ, listed in Table II. The inset shows important transitions and branching ratios used for the fit. Photopeak locations of important transitions are indicated by arrows.

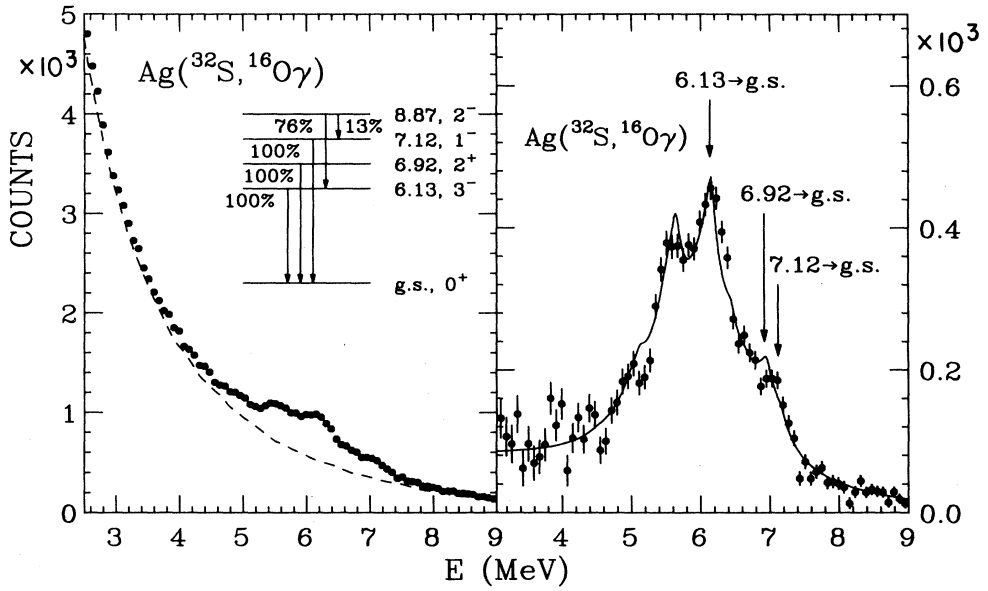

FIG. 19. γ-ray spectra measured in coincidence with ^{16}O fragments. The left-hand panel shows the raw coincidence spectrum with the background indicated by the dashed line. The right-hand panel shows the spectrum associated with γ-ray decays of excited ^{16}O fragments. The solid line shows the fit used for the extraction of the γ-ray fractions, F_γ, listed in Table II. The inset shows important transitions and branching ratios used for the fit. Photopeak locations of important transitions are indicated by arrows.

less than 8%. This extreme error estimate, however, was not incorporated into the uncertainties listed in Table II.

V. FEEDING FROM HIGHER-LYING STATES

The relative populations of states of the emitted fragments provide a measure of the intrinsic excitation energy of the emitting system at freezeout. It is important to know whether this excitation energy is thermally distributed. This can be explored by direct measurements of the relative populations of excited states. However, the observed populations of excited states are influenced by the sequential decay of heavier particle unstable nuclei,[28,31,48–50,63] and the populations and decays of many

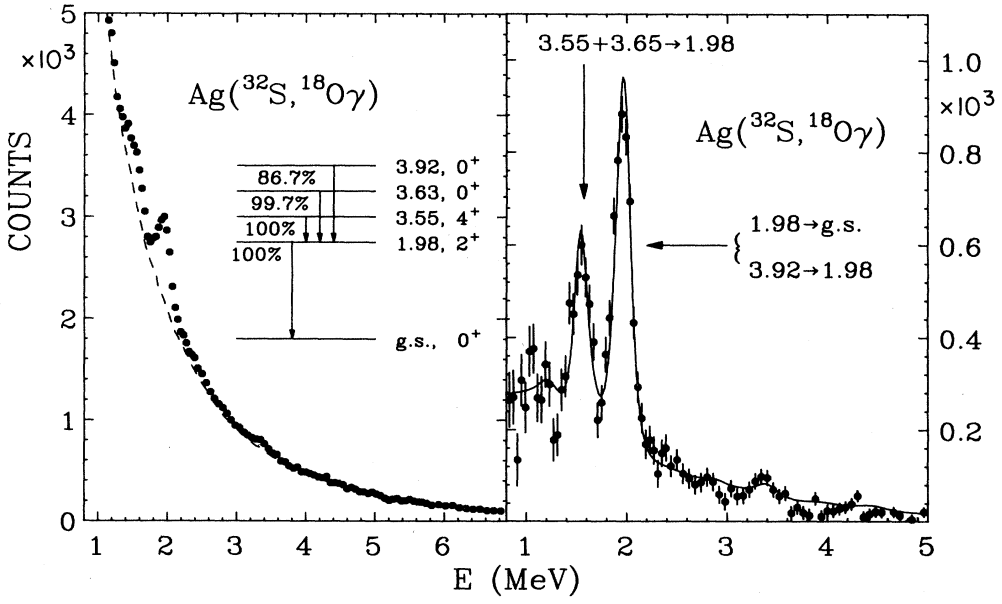

FIG. 20. γ-ray spectra measured in coincidence with ^{18}O fragments. The left-hand panel shows the raw coincidence spectrum with the background indicated by the dashed line. The right-hand panel shows the spectrum associated with γ-ray decays of excited ^{18}O fragments. The solid line shows the fit used for the extraction of the γ-ray fractions, F_γ, listed in Table II. The inset shows important transitions and branching ratios used for the fit. Photopeak locations of important transitions are indicated by arrows.

of these unbound states are not known experimentally. Since one does not usually know the feeding corrections experimentally, they must be calculated. These calculations[31,48,49] usually make the simplifying assumption that the states[67] of primary fragments are populated according to a thermal distribution characterized by a temperature, T. The accuracy of this assumption must be checked by comparing the calculations to the experimental data.

To determine the feeding corrections to the measured γ-ray fractions, we performed sequential decay calculations for an ensemble of nuclei with $3 \leq Z \leq 13$. Since the spins, isospins, and parities of many low-lying particle bound and unbound levels of nuclei with $Z \leq 11$ are known,[67] the information for these lighter nuclei was used in the sequential decay calculations. For known levels with incomplete spectroscopic information, values for the spin, isospin, and parity were chosen randomly according to primary distributions obtained from the noninteracting shell model.[68] These calculations were repeated with different initialization for the unknown spec-

TABLE II. Extracted fractions F_γ of observed fragments which were accompanied by the designated γ-ray transition. For transitions which could not be resolved experimentally, the F_γ value is given for the summed strength. These transitions and F_γ values are identified by subscripts "$\sum k$," $k = 1,2,\ldots,14$.

Fragment	Transition (J^π, E^*)	F_γ
^{7}Be	$(\frac{1}{2}^-, 0.429) \rightarrow (\frac{3}{2}^-, 0.0)$	0.222±0.017[a]
^{8}Li	$(1^+, 0.981) \rightarrow (2^+, 0.0)$	0.204±0.033[a]
^{10}Be	$(2^+, 3.37) \rightarrow (0^+, 0.0)$	0.61±0.03
	$(2^+, 5.96) \rightarrow (2^+, 3.37)_{\sum 1}$	0.16±0.02 $\left[\sum 1\right]$
	$(1^-, 5.96) \rightarrow (2^+, 3.37)_{\sum 1}$	
^{10}B	$(1^+, 2.154) \rightarrow (0^+, 1.740)$	0.082±0.015[a]
^{11}B	$(\frac{1}{2}^-, 2.12) \rightarrow (\frac{3}{2}^-, 0.0)$	0.110±0.015
	$(\frac{5}{2}^-, 4.44) \rightarrow (\frac{3}{2}^-, 0.0)$	0.143±0.016
	$(\frac{3}{2}^-, 5.02) \rightarrow (\frac{3}{2}^-, 0.0)$	0.059±0.008
	$(\frac{7}{2}^-, 6.74) \rightarrow (\frac{3}{2}^-, 0.0)_{\sum 2}$	0.135±0.028 $\left[\sum 2\right]$
	$(\frac{1}{2}^+, 6.79) \rightarrow (\frac{3}{2}^-, 0.0)_{\sum 2}$	
	$(\frac{5}{2}^+, 7.29) \rightarrow (\frac{3}{2}^-, 0.0)_{\sum 2}$	
	$(\frac{3}{2}^+, 7.98) \rightarrow (\frac{3}{2}^-, 0.0)_{\sum 2}$	
^{11}C	$(\frac{1}{2}^-, 2.00) \rightarrow (\frac{3}{2}^-, 0.0)$	0.151±0.028
	$(\frac{5}{2}^-, 4.32) \rightarrow (\frac{3}{2}^-, 0.0)_{\sum 3}$	0.133±0.016 $\left[\sum 3\right]$
	$(\frac{1}{2}^+, 6.34) \rightarrow (\frac{1}{2}^-, 2.00)_{\sum 3}$	
	$(\frac{3}{2}^-, 4.80) \rightarrow (\frac{3}{2}^-, 0.0)$	0.062±0.013
	$(\frac{1}{2}^+, 6.34) \rightarrow (\frac{3}{2}^-, 0.0)_{\sum 4}$	0.219±0.032 $\left[\sum 4\right]$
	$(\frac{7}{2}^-, 6.48) \rightarrow (\frac{3}{2}^-, 0.0)_{\sum 4}$	
	$(\frac{5}{2}^+, 6.90) \rightarrow (\frac{3}{2}^-, 0.0)_{\sum 4}$	
	$(\frac{3}{2}^+, 7.50 \rightarrow (\frac{3}{2}^-, 0.0)_{\sum 4}$	
^{12}B	$(2^+, 0.953) \rightarrow (1^+, 0.0)_{\sum 5}$	0.415±0.054[a] $\left[\sum 5\right]$
	$(1^-, 2.621) \rightarrow (2^-, 1.674)_{\sum 5}$	0.43±0.09 $\left[\sum 5\right]$
	$(2^-, 1.674) \rightarrow (1^+, 0.0)_{\sum 6}$	0.28±0.04 $\left[\sum 6\right]$
	$(1^-, 2.621) \rightarrow (2^+, 0.953)_{\sum 6}$	
^{12}C	$(2^+, 4.44) \rightarrow (0^+, 0.0)$	0.406±0.030
^{13}C	$(\frac{5}{2}^+, 3.854) \rightarrow (\frac{3}{2}^-, 3.684)$	0.070±0.009[a]
	$(\frac{5}{2}^+, 3.85) \rightarrow (\frac{1}{2}^-, 0.0)_{\sum 7}$	0.370±0.029 $\left[\sum 7\right]$
	$(\frac{3}{2}^-, 3.68) \rightarrow (\frac{1}{2}^-, 0.0)_{\sum 7}$	
	$(\frac{1}{2}^+, 3.09) \rightarrow (\frac{1}{2}^-, 0.0)_{\sum 7}$	

TABLE II. (*Continued*).

Fragment	Transition (J^π, E^*)	F_γ
^{14}C	$(1^-,6.09)\rightarrow(0^+,0.0)_{\Sigma 8}$	0.481 ± 0.040 $\left[\Sigma 8\right]$
	$(3^-,6.73)\rightarrow(0^+,0.0)_{\Sigma 8}$	
	$(2^+,7.01)\rightarrow(0^+,0.0)_{\Sigma 8}$	
	$(2^-,7.34)\rightarrow(0^+,0.0)_{\Sigma 8}$	
^{14}N	$(0^+,2.31)\rightarrow(1^+,0.0)$	0.165 ± 0.030
	$(1^+,3.95)\rightarrow(0^+,2.31)$	0.062 ± 0.040
	$(0^-,4.92)\rightarrow(1^+,0.0)_{\Sigma 9}$	0.216 ± 0.021 $\left[\Sigma 9\right]$
	$(2^-,5.11)\rightarrow(1^+,0.0)_{\Sigma 9}$	
	$(1^-,5.69)\rightarrow(1^+,0.0)_{\Sigma 9}$	
	$(3^-,5.83)\rightarrow(1^+,0.0)_{\Sigma 9}$	
	$(1^+,6.20)\rightarrow(1^+,0.0)_{\Sigma 9}$	
	$(3^+,6.44)\rightarrow(1^+,0.0)_{\Sigma 9}$	
	$(2^+,7.03)\rightarrow(1^+,0.0)_{\Sigma 9}$	
^{15}N	$(\frac{5}{2}^+,5.27)\rightarrow(\frac{1}{2}^-,0.0)_{\Sigma 10}$	0.391 ± 0.042 $\left[\Sigma 10\right]$
	$(\frac{1}{2}^+,5.30)\rightarrow(\frac{1}{2}^-,0.0)_{\Sigma 10}$	
	$(\frac{5}{2}^+,7.16)\rightarrow(\frac{5}{2}^+,5.27)_{\Sigma 11}$	0.165 ± 0.040 $\left[\Sigma 11\right]$
	$(\frac{7}{2}^+,7.57)\rightarrow(\frac{5}{2}^+,5.27)_{\Sigma 11}$	
^{16}O	$(3^-,6.13)\rightarrow(0^+,0.0)$	0.220 ± 0.025
	$(2^+,6.92)\rightarrow(0^+,0.0)_{\Sigma 12}$	0.146 ± 0.024 $\left[\Sigma 12\right]$
	$(1^-,7.12)\rightarrow(0^+,0.0)_{\Sigma 12}$	
^{18}O	$(2^+,1.98)\rightarrow(0^+,0.0)_{\Sigma 13}$	0.75 ± 0.07 $\left[\Sigma 13\right]$
	$(2^+,3.92)\rightarrow(2^+,1.98)_{\Sigma 13}$	
	$(4^+,3.55)\rightarrow(2^+,1.98)_{\Sigma 14}$	0.27 ± 0.06 $\left[\Sigma 14\right]$
	$(0^+,3.63)\rightarrow(2^+,1.98)_{\Sigma 14}$	

[a]These values are taken from Ref. 31 and corrected for the effects of coincidence summing.

troscopic information until the sensitivities of the calculations to these uncertainties could be assessed. The results of the calculations appear to be insensitive to details in the sampling algorithm, and essentially the same results were obtained in simpler calculations where spins of 0–4 ($\frac{1}{2}$–$\frac{9}{2}$) were assumed with equal probability for even-A (odd-A) nuclei, parities were assumed to be odd or even with equal probability, and the isospins were assumed to be given by the isospin of the ground state. For later reference, this latter distribution of unknown spins is termed as "flat spin distribution."

The low-lying discrete levels of heavier nuclei with $Z \geq 12$ are not as well known. To calculate the decay of these heavier nuclei for low excitation energies, $E^* \leq \varepsilon_0$, we used a continuum approximation to the discrete level density,[69] modifying the empirical interpolation formula of Ref. 70 to include a spin dependence

$$\rho(E^*,J_i)=\frac{1}{T_1}\exp[(E^*-E_1)/T_1] \times \frac{(2J_i+1)\exp[-(J_i+\frac{1}{2})^2/2\sigma_i^2]}{\sum(2J_i+1)\exp[-(J_i+\frac{1}{2})^2/2\sigma_i^2]}, \quad \text{for } E^* \leq \varepsilon_0 , \tag{3}$$

where

$$\sigma_i^2=0.0888[a_i(\varepsilon_0-E_0)]^{1/2}A_i^{2/3} , \tag{4}$$

and $a_i=A_i/8$; J_i, A_i, and Z_i are the spin, mass, and charge numbers of the fragment, and the values for $\varepsilon_0=\varepsilon_0(A_i,Z_i)$, $T_1=T_1(A_i,Z_i)$, and $E_1=E_1(A_i,Z_i)$ were taken from Ref. 70. For $Z_i \geq 12$, $E_0=E_0(A_i,Z_i)$ is

determined by matching the level density provided by Eq. (3) at ε_0 to that provided by Eq. (5). [Note: In Eq. (3) and also in Eq. (9), we match the density of levels rather than the density of states because the spins of many of the discrete levels are not known.]

For higher excitation energies in the continuum for all nuclei, we assumed the level density of the form

$$\rho(E^*,J_i)=\rho_1(E^*)\rho_2(J_i,\sigma_i) , \tag{5}$$

where

$$\rho_1(E^*)=\frac{\exp\{2[a_i(E^*-E_0)]^{1/2}\}}{12\sqrt{2}[a_i(E^*-E_0)^5]^{1/4}\sigma_i} , \tag{6}$$

$$\rho_2(J_i,\sigma_i)=\frac{(2J_i+1)\exp[-(J_i+\frac{1}{2})^2/2\sigma_i^2]}{2\sigma_i^2} , \tag{7}$$

$$\sigma_i^2=0.0888[a_i(E^*-E_0)]^{1/2}A_i^{2/3} . \tag{8}$$

For $Z_i \geq 12$, $E_0=E_0(A_i,Z_i)$ is determined by matching the level density provided by Eq. (3) at ε_0 to that provided by Eq. (5). At smaller values of Z_i, E_0 is adjusted for each fragment to match the integral of the continuum level density to the total number of tabulated levels according to the equation

$$\int_{E_0}^{\varepsilon_0} dE^* \int dJ\, \rho(E^*,J)=\int_0^{\varepsilon_0} dE^* \sum_i \delta(E_i-E^*) , \tag{9}$$

where ε_0, for these lighter fragments, was chosen to be the maximum excitation energy up to which the information concerning the number and locations of discrete states appears to be complete. To reduce the computer memory requirements, the populations of continuum states were stored at discrete excitation energy intervals of 1 MeV for $E^* \leq 15$ MeV, 2 MeV for $15 \leq E^* \leq 30$ MeV, and 3 MeV for $E^* \geq 30$ MeV. The results of these calculations do not appear to be sensitive to these binning widths. Parities of states described in Eqs. (3) and (5) were chosen to be positive and negative with equal probability. To save both space and time, the isospins of the continuum states were taken to be equal to the isospin of the ground state of the same nucleus.

For the ith level of spin J_i we assumed an initial population P_i, given by

$$P_i \propto P_0(A_i,Z_i)(2J_i+1)\exp(-E^*/T) , \tag{10}$$

where $P_0(A_i,Z_i)$ denotes the population per spin degree of freedom of the ground state of a fragment and T is the emission temperature which characterizes the thermal population of states of a given isotope. (This temperature is associated with the intrinsic excitation of the fragmenting system at breakup and is, in general, different from the "kinetic" temperature which may be extracted from the kinetic-energy spectra of the emitted fragments.) The initial populations of states of a given fragment were assumed to be thermal up to excitation energies of $E^*_{\text{cutoff}}=\mu A$. This cutoff was introduced to explore the sensitivity of the calculations to highly excited and short-lived nuclei, some of which may be too short lived to survive the evolution from breakup to freezeout. Calculations were performed for cutoff values of $\mu=3$ and 5

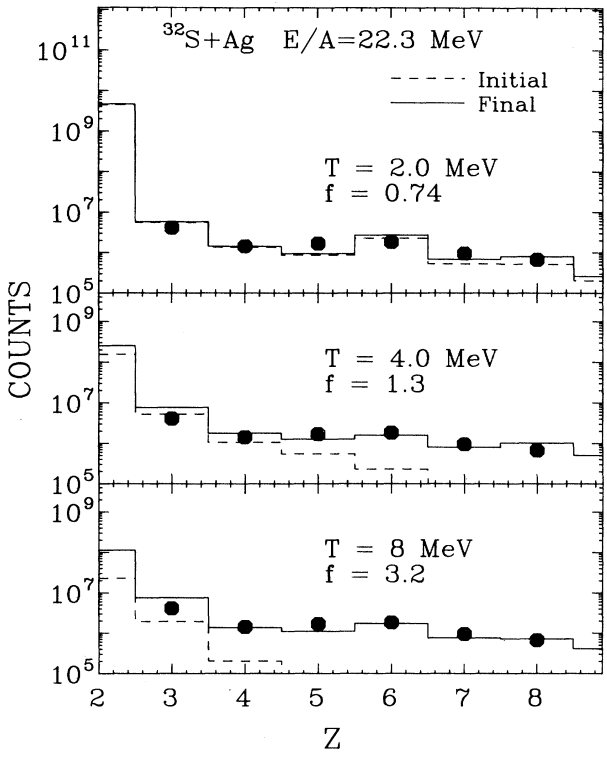

FIG. 21. Element yields summed over all measured energies and angles. The dashed and solid histograms show the primary and final fragment particle stable yields for the feeding calculations described in the text. The three panels show the results for $T=2$, 4, and 8 MeV, respectively. The adjusted values of the parameter f in Eq. (11) are given in the figure.

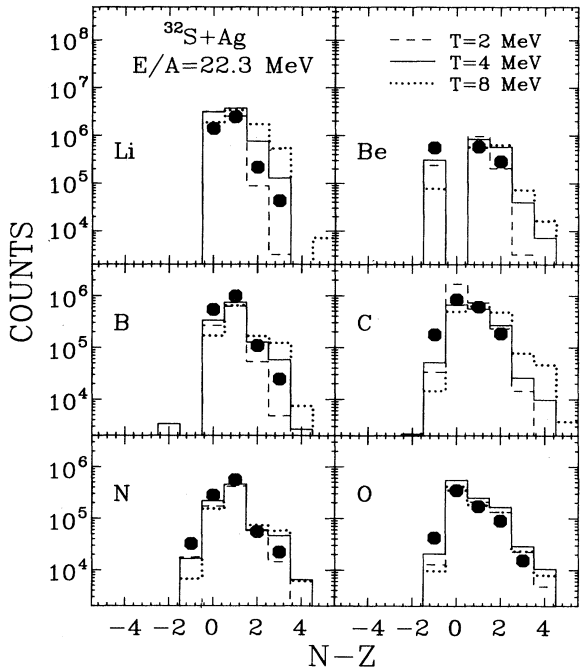

FIG. 22. Isotope yields summed over all measured energies and angles. The dashed, solid, and dotted histograms show the final fragment distributions for the feeding calculations at $T=2$, 4, and 8 MeV, respectively.

MeV corresponding to mean lifetimes of the continuum states of 230 and 125 fm/c, respectively.[71] The calculations were qualitatively similar for the two cutoff energies.

For simplicity, we parametrize the initial relative populations, $P_0(A_i,Z_i)$, by

$$P_0(A,Z) \propto \exp(-fV_C/T+Q/T) , \tag{11}$$

where V_C is the Coulomb barrier for emission from a parent nucleus of mass and atomic numbers A_p and Z_p and Q is the ground state Q value

$$V_C = Z_i(Z_p-Z_i)e^2/\{r_0[A_i^{1/3}+(A_p-A_i)^{1/3}]\} \tag{12}$$

and

$$Q = [B(A_p-A_i,Z_p-Z_i)+B_i]-B(A_p,Z_p) . \tag{13}$$

We used the radius parameter of $r_0=1.2$ fm. The binding energies $B(A,Z)$ of heavy nuclei were calculated from the Weizsäcker mass formula.[72] For the emitted light fragments we used the measured binding energies B_i of the respective ground states. At each temperature, the parameter f in Eq. (11) was adjusted to provide optimal agreement between the calculated final fragment distributions (obtained after the decay of particle unstable states) and the measured fragment distributions. This constraint reduced the possibility of inaccuracies in the predicted primary elemental distributions at high temperatures.[48,49]

If known, tabulated branching ratios were used to describe the decay of particle unstable states; if unknown, the branching ratios were calculated from the Hauser-Feshbach formula[73,74]

$$\frac{\Gamma_c}{\Gamma} = \frac{G_c}{\sum_i G_i} , \tag{14}$$

where

$$G_c = \langle T_{I,D}T_{I,F}T(3)_{I,D}T(3)_{I,F}|T_{I,P}T(3)_{I,P}\rangle^2 \times \sum_{Z=|S-j|}^{Z=S+j}\sum_{l=|J-Z|}^{l=J+Z}[1+\pi_P\pi_D\pi_F(-1)^l]/2T_l(E) . \tag{15}$$

Here, J and j are the spins of the parent and daughter nuclei, Z is the channel spin, S and l are the intrinsic spin and orbital angular momentum of the emitted particle, and $T_l(E)$ is the transmission coefficient for the lth partial wave. The factor $[1+\pi_P\pi_D\pi_F(-1)^l]/2$ enforces parity conservation and depends on the parities $\pi=\pm1$ of the emitted fragment and the parent and daughter nuclei. The Clebsch-Gordan coefficient involving $T_{I,P}$, $T_{I,D}$, and $T_{I,F}$, the isospins of the parent nucleus, daughter nucleus, and emitted particle, likewise allows one to take isospin conservation into account. For decays from continuum states when the kinetic energy of the emitted particle exceeds 20 MeV, the transmission coefficients were approximated by the sharp cutoff approximation; otherwise, the transmission coefficients were interpolated[74] from a set of calculated optical model transmission coefficients.

The measured fragment elemental and isotopic distributions and calculated distributions for $\mu=3$ MeV are compared in Figs. 21 and 22. The solid circles correspond to the fragment yields summed over all measured energies and angles. The dashed lines in Fig. 21 show the calculated elemental distributions of primary fragments (summation of all particle stable states for all isotopes of a given element) assumed for the temperatures $T=2$, 4, and 8 MeV; the parameters f are indicated in the figure. The solid lines show the calculated final elemental distributions obtained after the statistical decay of particle unbound fragments. The parameter f was adjusted at each temperature so that the calculated final elemental distribution closely follows the trend of the measured elemental distribution. (After choosing appropriate but different values for f, very similar results were also obtained for $\mu=5$ MeV.) Since these parameters, f, have been adjusted to reproduce the elemental yields measured in *this* experiment, one must be very cautious about applying the results of these calculations to other reactions.

The dashed, solid, and dotted histograms in Fig. 22 represent final isotopic distributions obtained for the three temperatures, $T=2$, 4, and 8 MeV, using the parameters f given in Fig. 21. In general, the isotopic distributions are fairly well reproduced. For $T=2$ MeV, however, the calculated isotopic distributions are somewhat narrower than the measured ones and for $T=8$ MeV, the calculated distributions are somewhat broader than the measured ones. The agreement is slightly better for calculations in the neighborhood of $T\approx4$ MeV.

VI. MEAN EMISSION TEMPERATURES

Starting from the initial distribution, Eq. (10), we have calculated the fraction F_γ of γ rays emitted in coincidence with a given fragment as a function of the emission temperature T which characterizes the ensemble of emitted fragments. The results for an excitation energy cutoff of $\mu=3$ MeV are presented in Figs. 23–25 for the transitions given in the individual panels. The range of calculated fractions F_γ for individual γ rays are bounded by the solid curves in Figs. 23 and 24 for transitions measured in this experiment. The range of calculated values for the relative γ-ray intensities, $R_\gamma=F_{\gamma1}/F_{\gamma2}$, are shown by the solid lines in Fig. 25 for those fragments for which more than one γ-ray transition were measured. The corresponding calculations for an excitation energy cutoff of $\mu=5$ MeV are qualitatively very similar and in some cases, indistinguishable.

The spread in calculated values of F_γ's and R_γ's shown in Figs. 23–25 reflect primarily the uncertainties in the calculations coming from uncertainties in the spins, isospins, and parities of many low-lying particle unstable levels which directly feed the particle stable states of interest. The range of calculated values was determined by repeating the calculation with different spectroscopic assumptions until the sensitivity of the calculation to those uncertainties could be assessed.

In order to illustrate the modifications due to feeding from particle unbound states, the dashed lines in Figs. 23–25 show the results of calculations which include feeding from higher-lying particle stable states, but not from particle unstable states. In all cases, both F_γ's and

R_γ's are predicted to be sensitive to feeding from particle unbound states for temperatures higher than approximately 2–3 MeV (for example, for ^{11}C with $\mu=3$ MeV and $T=3$ Mev, 55% of the yields of the 4.32-MeV excited state and 59% of the ground-state yields are predicted to proceed through the sequential decay of heavier particle unbound nuclei). R_γ has the advantage of being independent of the total feeding to the ground states of the observed fragments. Since the ground state is fed more strongly than the excited states, the R_γ's are slightly less sensitive to the uncertainties in the sequential decay corrections than the F_γ's shown in Figs. 23 and 24.

The shaded horizontal bands in Figs. 23–25 correspond to the experimental values of F_γ and R_γ, respectively, that are obtained when the data for different intermediate mass fragment kinetic energies and scattering angles are combined. In general, the experimental data are larger than the calculations for emission temperatures less than

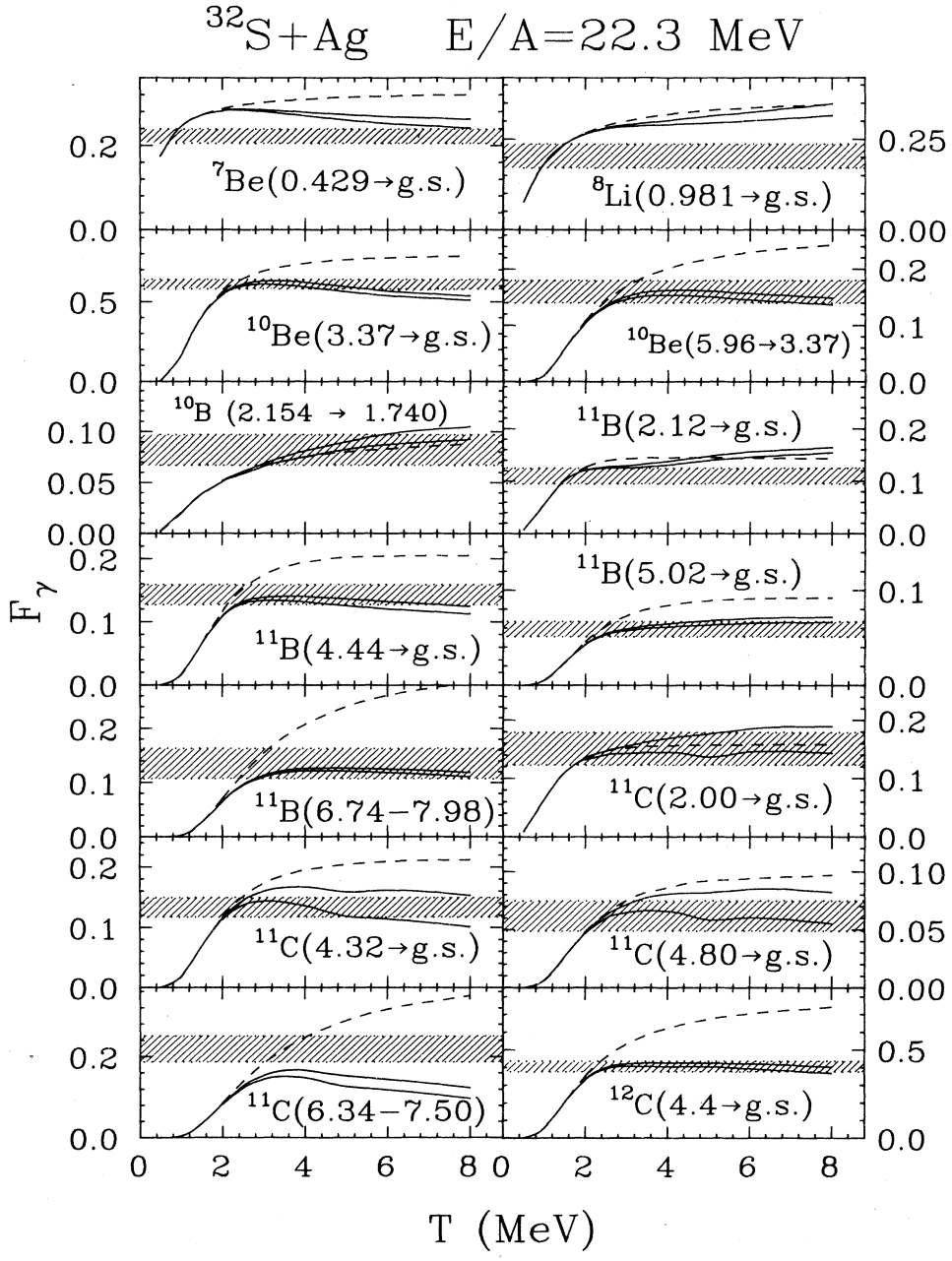

FIG. 23. The solid curves indicate the range of calculated fractions F_γ for fragments decaying through the designated γ-ray transition as a function of the emission temperature T which characterizes the ensemble of emitted fragments. (The values for F_γ on the curves are one theoretical standard deviation from the average value of F_γ provided by the calculations.) The dashed lines show the fractions calculated when feeding from particle stable states is included, but not feeding from particle unbound states. The horizontal bands indicate the measured values.

2 MeV. For most transitions at temperatures of about 3 to 4 MeV, the range of calculated values lie within 20% of the range of experimental values permitted by our estimate of the experimental uncertainties. However, at these and higher temperatures, the calculations are not very sensitive to temperature, making it impossible to extract reliable upper limits based on individual cases. Some of the transitions, e.g., the F_γ's for ^{8}Li(0.98→g.s.), ^{15}N(5.27+5.30→g.s.), ^{16}O(6.13→g.s.), and the ratio R_γ ($=F_{\gamma 2}/F_{\gamma 1}$) for ^{11}C(6.34−7.50→g.s./4.32→g.s.), deviate significantly from the overall trends, with the ranges of calculated and measured values in disagreement by more than 20% at temperatures of 3–4 MeV. Such discrepancies could be due to inaccuracies in the spectroscopic information that influence strongly the calculations for these nuclei, or could be indicative of non-

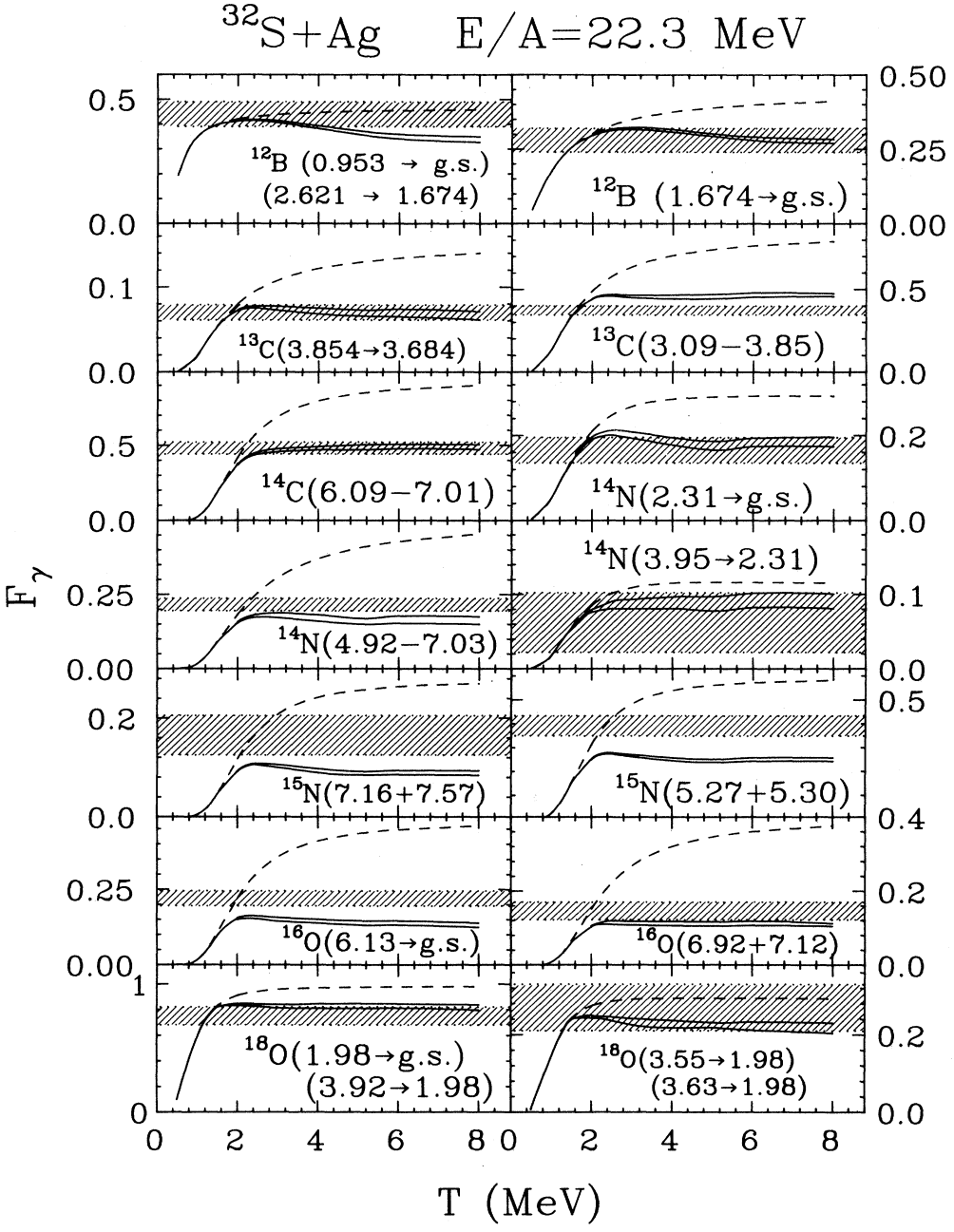

FIG. 24. The solid curves indicate the range of calculated fractions F_γ for fragments decaying through the designated γ-ray transition as a function of the emission temperature T which characterizes the ensemble of emitted fragments. (The values for F_γ on the curves are one theoretical standard deviation from the average value of F_γ provided by the calculations.) The dashed lines show the fractions calculated when feeding from particle stable states is included, but not feeding from particle unbound states. The horizontal bands indicate the measured values.

thermal excited state populations either in these nuclei or in heavier nuclei which feed these transitions by sequential decay processes.

To provide a more quantitative comparison between calculations and experimental data, we have performed a least-squares analysis, computing the function,

$$\chi_\nu^2=\frac{1}{\nu}\sum_i^{\nu}\frac{(y_{\mathrm{exp},i}-y_{\mathrm{cal},i})^2}{\sigma_i^2}\ , \tag{16}$$

where $y_{\mathrm{exp},i}$ and $y_{\mathrm{cal},i}$ are the ith experimental and calculated values of the γ-ray fraction, F_γ, or the ratio of γ-ray fractions, R_γ; ν is the number of independent data points ($\nu=28$ for F_γ's, and $\nu=12$ for R_γ's); and σ_i, given by $\sigma_i^2=\sigma_{\mathrm{exp},i}^2+\sigma_{\mathrm{cal},i}^2$ is an uncertainty associated with the comparison for the ith measured quantity. In the latter expression, $\sigma_{\mathrm{exp},i}$ is the experimental uncertainty; $\sigma_{\mathrm{cal},i}$ reflects the range of calculated values corresponding to the different assumptions for the spins, isospins, and parities of low-lying states where this information is incomplete. $\sigma_{\mathrm{cal},i}^2$ was computed as the variance of the calculations indicated in Figs. 23–25.

Values for χ_ν^2 calculated for the γ-ray fractions in Figs. 23 and 24 are shown on the right-hand side of Fig. 26. Values for χ_ν^2 calculated for the ratios of γ-ray fractions given in Fig. 25 are shown on the left-hand side of Fig.

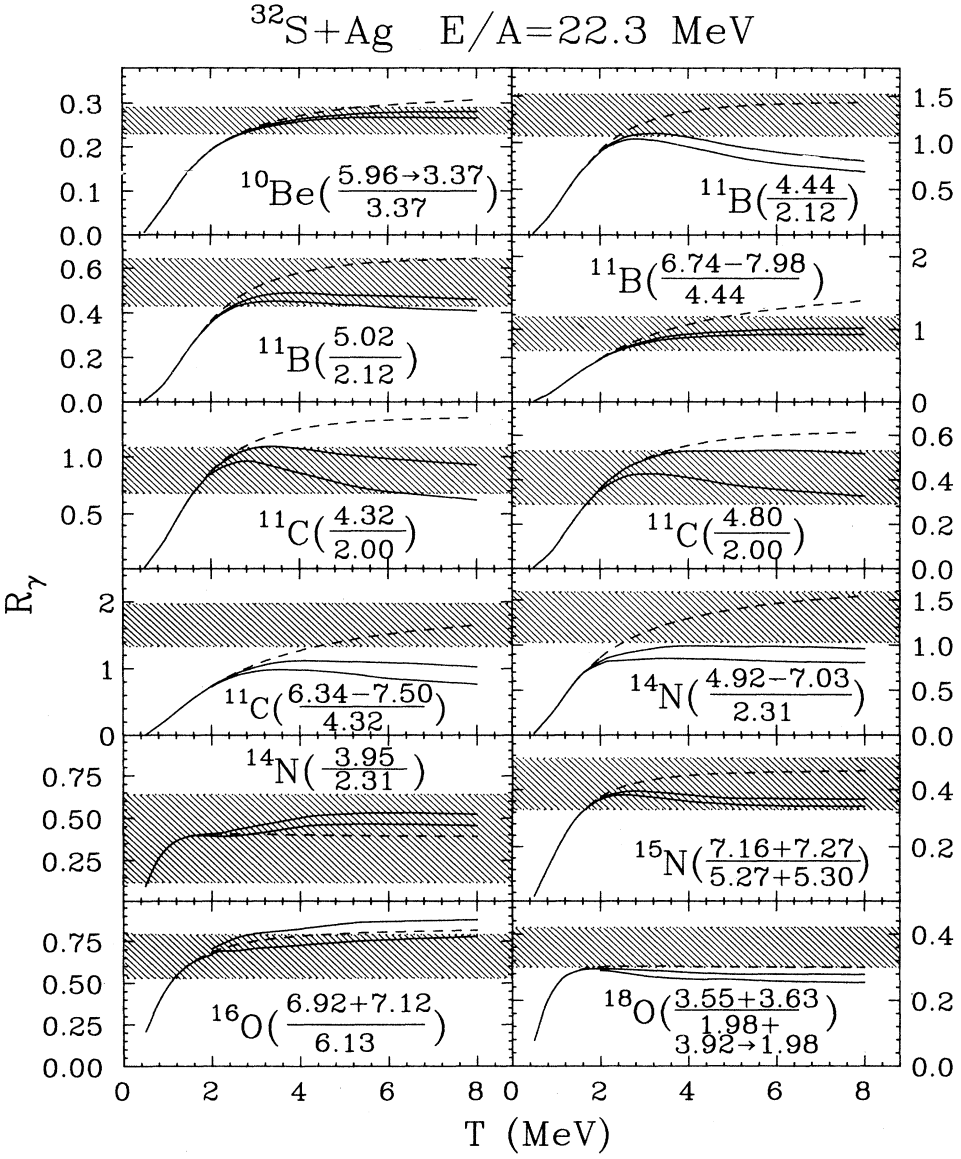

FIG. 25. The solid curves indicate the range of calculated fractions, $R_\gamma=F_{\gamma 1}/F_{\gamma 2}$, of designated γ-ray transition probabilities as a function of the emission temperature T which characterizes the ensemble of emitted fragments. (The values for R_γ on the curves are one theoretical standard deviation from the average value of R_γ provided by the calculations.) The dashed lines show the ratios calculated when feeding from particle stable states is included, but not feeding from particle unbound states. The horizontal bands indicate the measured values.

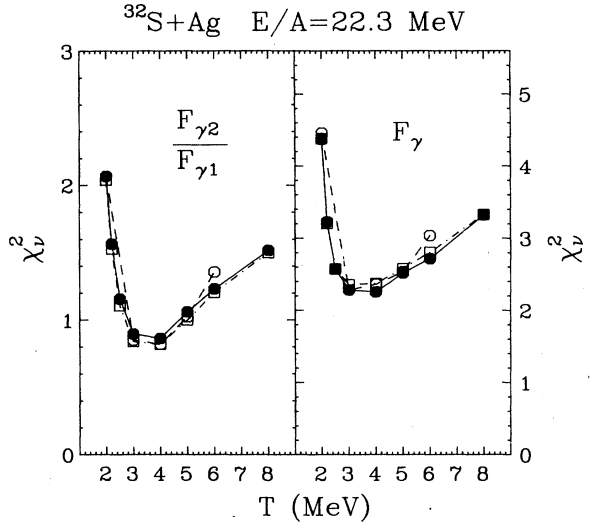

FIG. 26. Left-hand side: Results of the least-squares analysis of the ratios of γ-ray fractions R_γ. Right-hand side: Results of the least-squares analysis of the γ-ray fractions F_γ. The solid and open circles depict the values for χ^2_ν obtained for excitation energy cutoffs of $\mu=3$ and 5 MeV, respectively, when the unknown spectroscopic information for low-lying discrete states was chosen according to the noninteracting shell model. The open squares depict the values for χ^2_ν obtained for an excitation energy cutoff of $\mu=3$ MeV when the unknown spectroscopic information for low-lying discrete states was chosen according to the simpler "flat spin distribution" described in Sec. V. The lines connecting respective points are used to guide eyes.

26. The solid and open circles depict the values for χ^2_ν obtained for excitation energy cutoffs of $\mu=3$ and 5 MeV, respectively, when the unknown spectroscopic information for low-lying discrete states was chosen according to the noninteresting shell model. The open squares depict the values for χ^2_ν obtained for an excitation energy cutoff of $\mu=3$ MeV when the unknown spectroscopic information for low-lying discrete states was chosen according to the simpler "flat spin distribution" described in Sec. V. For all calculations, minimum values for χ^2_ν are observed in the region of $T=3$–4 MeV for both sets of measurements. The comparison involving ratios of γ-ray fractions may be slightly more accurate because such ratios are insensitive to uncertainties in the ground-state yields, for which much more sequential feeding contributions are observed in these and other similar calculations.[31,48,49,69] This argument is supported by the values of the reduced χ^2 indicated in the figure. For the comparison involving ratios of γ-ray fractions, the minimum value of χ^2_ν approaches unity, corresponding to statistical agreement between calculations and measurements. χ^2_ν is larger for comparisons involving γ-ray fractions alone. This larger value of χ^2_ν may be partly attributed to a small number of transitions where the disagreements between measured and calculated values of F_γ are especially large. Some of these transitions (e.g., in ^{8}Li, ^{15}N, and ^{16}O fragments) were identified previously. Both calculations appear to exclude temperatures much larger than 5 MeV or smaller than 3 MeV. The upper limit is, however, much less certain because the feeding corrections are larger and the calculations less sensitive to temperature at higher excitation energies.

VII. SUMMARY AND CONCLUSIONS

We have investigated the emission of intermediate mass fragments for ^{32}S induced reactions on ^{nat}Ag at $E/A=22.3$ MeV. Inclusive energy spectra and angular distributions were measured for isotopically resolved fragments with $Z=3$–8. The energy spectra exhibit broad maxima at energies close to the exit channel Coulomb barriers and nearly exponential tails at higher energies. The slopes of the energy spectra become steeper at larger emission angles. The angular distributions of the emitted fragments are forward peaked in the center-of-mass frame indicating significant emission prior to the attainment of statistical equilibrium of the composite system.

Information about the populations of particle stable states of the emitted fragments was obtained by measuring their γ-ray decays with the spin spectrometer. A total of 28 independent γ-ray transition intensities were measured for fragments of mass $A=7$–18.

The effects of feeding from particle unbound states were investigated by calculations in which the initial populations of particle bound and unbound states, both discrete and continuum, of fragments with $Z\leq 13$ were assumed to be thermally populated. The decay of these fragments was calculated by using experimentally known γ-ray branching ratios and particle decay branching ratios. When branching ratios for the decays of particle unstable states were unknown, they were calculated from the statistical model. The primary fragment distributions were adjusted such that, after the decays of particle unstable states, the calculated final fragment yields were consistent with the measured yields. Unknown spins and parities of low-lying discrete particle unbound states were chosen randomly according to a distribution defined by the noninteracting shell model. Repeating the calculations with different choices for this spectroscopic information gave a range of calculated γ-ray fractions and ratios of γ-ray fractions. This provided a measure of the theoretical uncertainty associated with the lack of spectroscopic information. It remains an open question, however, whether a more accurate description of the isospin and parity dependence of the level densities could result in significantly different predictions for specific transitions.

No significant dependence of the measured γ-ray intensities upon the fragment energy or angle of emission was observed. When the experimental data for all angles and energies was combined, a large number of γ-ray intensities can be rather well described by these calculations for emission temperatures ranging from 3–4 MeV. This result is significant since it allows the description of a large number of measured values in terms of a single parameter. This, ultimately, must be the experimental justification of statistical treatments. This result therefore adds support for statistical treatments of the fragmentation process and for a thermal description of the

primary distribution. A few of the measured γ-ray intensities strongly disagree with the calculated γ-ray intensities at temperatures of about 3–4 MeV. Because all of the measured γ-ray transitions are strongly fed at high excitation energies, however, the present level of agreement between calculations and measurements may reflect more the accuracy of the sequential decay calculations than the accuracy of the thermal description of the primary distribution. Significant discrepancies between the actual primary distributions and thermal predictions may be better revealed by measurements of higher lying particle unbound states that are less strongly fed.[75]

ACKNOWLEDGMENTS

We wish to acknowledge many helpful discussions with T. Murakami. This work was supported by the National Science Foundation under Grant Nos. PHY-83-12245 and PHY-86-11210, by the U.S. Department of Energy under Contract No. DE-AC05-84OR21400 with Martin Marietta Energy Systems, and Nos. DE-AS02-76ER04052 and DE-AC02-85ER40210 with the Office of High Energy and Nuclear Physics. J.P. acknowledges the receipt of a fellowship from the Deutsche Forschungsgemeinschaft (West Germany). W.G.L. and L.G.S. acknowledge the receipt of U.S. Presidential Young Investigator Awards.

APPENDIX: γ-RAY CALIBRATIONS

1. Line-shape calibration

The response functions for the individual detector modules of the spin spectrometer were calibrated with γ rays emitted from ^{24}Na, ^{60}Co, ^{88}Y, and ^{207}Bi radioactive sources as well as γ rays produced by the inelastic scattering of protons on ^{12}C and ^{16}O nuclei. In total, 12 calibration points were measured over the energy range of $E_\gamma \approx 0.57$–7 MeV.

After gain matching of the individual detector modules, the γ-ray spectra were summed over the detectors located in the back hemisphere of the spin spectrom-

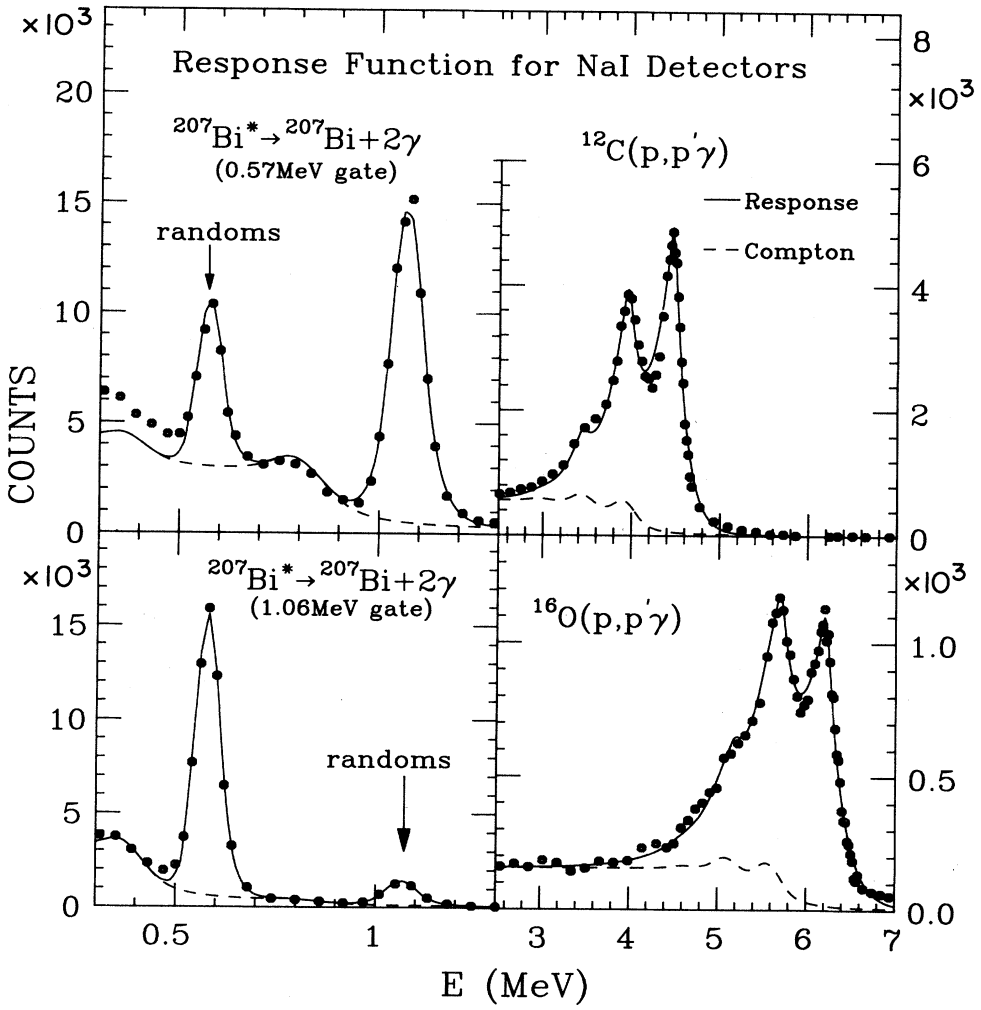

FIG. 27. Calibrations for the γ-ray response function, $\varepsilon_\gamma(E, E_0, A_0)$, given by Eqs. (A1)–(A3). The solid lines show the fitted line shapes; the dashed lines show the calculated Compton background.

eter The summed spectra were then fitted with a parametrized response function. Examples of calibration fits are shown in Fig. 27. The fitted response function was parametrized as

$$\varepsilon_\gamma(E,E_0,A_0)=\sum_{k=0}^{2} A_k[\alpha_k(E,E_k)+\beta_k(E,E_k)] \tag{A1}$$

with

$$\alpha_k(E,E_k)=\begin{cases}\exp[(L_k/2\sigma_k^2)(L_k+2E-2E_k)], & \text{for } E\le E_k-L_k\\ \exp[-(E-E_k)^2/2\sigma_k^2], & \text{for } E_k-L_k<E<E_k+U_k\\ \exp[(U_k/2\sigma_k^2)(U_k-2E+2E_k)], & \text{for } E\ge E_k+U_k\end{cases} \tag{A2}$$

and

$$\beta_k(E,E_k)=S_k\left\{\frac{\pi}{2}+\operatorname{arctg}[a_k(E-E_k-b_k)]+T_k\{\operatorname{arctg}[a_k(E-E_k-b_k-c)]-\operatorname{arctg}[a_k(E-E_k-b_k+c)]\}\right\} . \tag{A3}$$

In Eqs. (A1)–(A3), the indices $k=0$, 1, and 2 denote the photo, first, and second escape peaks, respectively; E_0 and E denote the original γ-ray energy and the detector response in MeV; the functions $\alpha_k(E,E_k)$ and $\beta_k(E,E_k)$ parametrize the line shapes of the individual peaks and the Compton backgrounds, respectively. The positions of the first and second escape peaks were given by

$$E_k=E_0-0.511k . \tag{A4}$$

The photopeak amplitude A_0 was fit to the measured spectrum, and the relative normalizations of the amplitudes, A_1 and A_2, were determined from the calibrations and could be expressed in the functional form

$$A_k=C_k A_0\{1-\exp[(1.56-E_k)/3.0]\}H(E_k-1.56) \quad (k=1,2) , \tag{A5}$$

where $H(x)$ is the unit step function, $H(x)=0$ for $x<0$ and $H(x)=1$ for $x>0$, and $C_1=0.90$ and $C_2=0.18$. The energy dependence of the line-shape parameters was determined by the calibrations and could be represented by the functions

$$L_k=[0.19+3.52\exp(-E_k)]\sigma_k , \tag{A6}$$

$$U_k=[0.47+1.22\exp(-E_k/1.91)]\sigma_k , \tag{A7}$$

$$\sigma_k=(6.8+33E_k^{1/2})\times 10^{-3} , \tag{A8}$$

$$S_k=\begin{cases}-0.012E_k+0.075, & \text{for } E_k\le 4.44 \text{ MeV}\\ 0.00345E_k+0.0063, & \text{for } E_k\ge 4.44 \text{ MeV} ,\end{cases} \tag{A9}$$

$$T_k=29.5\sigma_k , \tag{A10}$$

$$a_k=-1.0/(78.7\sigma_k) , \tag{A11}$$

$$b_k=-2.0-377.0\sigma_k+50.0E_k/(1.0+9.8E_k) , \tag{A12}$$

$$c=72.0\sigma_0 . \tag{A13}$$

Apart from the γ-ray energy E_0, the calibrated detector response function contains only the adjustable parameter A_0 which determines the normalization.

2. Absolute efficiency

The relation between the fitted amplitude A_0 and the total number of γ rays of energy E_0 was calibrated at low energies, $E_\gamma=0.57$–2.75 MeV, via γ-γ coincidence measurements using radioactive sources with coincident transitions. At higher energies, $E_\gamma\ge 4.4$ MeV, the absolute efficiency was obtained from p-γ coincidences measured for the inelastic scattering of protons on ^{12}C and ^{16}O. If the observed γ-ray peak can be attributed completely to the particle γ-ray coincidence yield, we can define the normalization function $\eta_\gamma(E_0)$ as

$$\eta_\gamma(E_0)=A_0(E_0)/N(E_0) , \tag{A14}$$

where $A_0(E_0)$ is the amplitude fitted to the spectrum of a γ ray of energy E_0 [defined as A_0 in Eq. (A1)] and $N(E_0)$ is the total number of emitted γ rays.

For two coincident γ rays of energies E_0 and E_0', the efficiency for the detection of γ rays of energy E_0 with the NaI(Tl) detectors of the spin spectrometer can be calibrated by determining the amplitude $A_0(E_0)$ for the spectrum measured in coincidence with γ rays of energy E_0' detected with a Compton suppressed Germanium detector module of the spin spectrometer. When gated on the γ-ray peak of energy E_0' in *one* (Ge) detector, non-negligible contributions, $A_0(E_0')$, of the *same* energy E_0' are observed in the *other* (NaI) detectors (Fig. 27). These contributions, $A_0(E_0')$, are entirely due to random coincidences and thus allow us to correct for the random coincidence contributions to the true peak $A_0(E_0)$. Since $A_0(E_0)$ is determined from the spectrum summed over all detectors contained in the backward hemisphere of the Spin Spectrometer, angular correlation effects are effectively integrated out. When such random coincidence effects are important, $\eta_\gamma(E_0)$ is not given by Eq. (A14). Instead, making the random correction, one has,

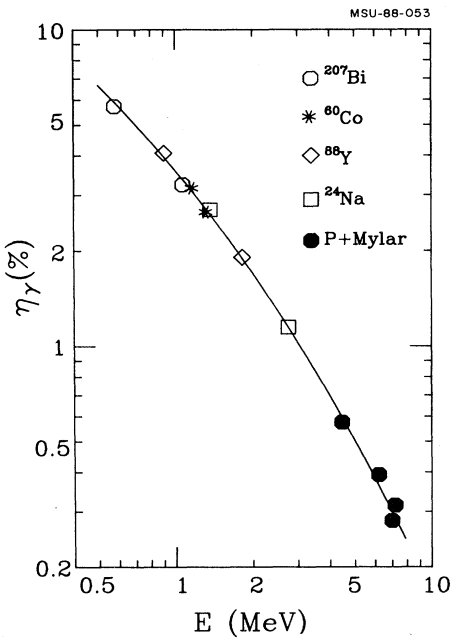

FIG. 28. Measured values of the normalization function $\eta_\gamma(E_0)$, defined in Eq. (A14)–(A16). The solid line corresponds to the analytic interpolation given by Eq. (A17).

$$\eta_\gamma(E_0)=\left[A_0(E_0)-A_0(E_0')\frac{\eta_\gamma(E_0)}{\eta_\gamma(E_0')}\frac{P_\gamma(E_0)}{P_\gamma(E_0')}\right]\times\frac{1}{N_{\mathrm{Ge}}(E_0')P_{\gamma\gamma}(E_0)}\ . \tag{A15}$$

Here, $N_{\mathrm{Ge}}(E_0')$ denotes the total number of γ rays of energy E_0' detected in the Germanium detector; $P_{\gamma\gamma}(E_0)$ denotes the conditional probability that a γ ray of energy E_0 is emitted in coincidence with the detected γ ray of energy E_0'; typically, $P_{\gamma\gamma}(E_0)\approx 0.8$–$1.0$; $P_\gamma(E_0)$ and $P_\gamma(E_0')$ correspond to the single inclusive emission probabilities for γ rays of energies E_0 and E_0', respectively. The second term in the square brackets corrects for random coincidences. When gated on the other γ-ray peak E_0 (Fig. 27, the upper and lower figures in the left-hand column), the true coincidence amplitude for γ rays of energy E_0' and random amplitude for γ rays of energy E_0 can be extracted. Thus, a corresponding equation for $\eta_\gamma(E_0')$ can be established with E_0 and E_0' interchanged in Eq. (A15), allowing the unambiguous determination of $\eta_\gamma(E_0)$ and $\eta_\gamma(E_0')$ by an iterative procedure.

For the case of γ rays emitted in the ^{12}C$(p,p'\gamma)$ and ^{16}O$(p,p'\gamma)$ reactions, one places a gate on the respective peak in the proton spectrum to determine the number $N_{p'}$ of inelastically scattered protons. Summing over the NaI(Tl) detectors in the backward hemisphere, one obtains

$$\eta_\gamma(E_0)=A_0(E_0)/[N_{p'}P_{p\gamma}(E_0)]\ , \tag{A16}$$

where the amplitude $A_0(E_0)$ is determined from the coincident γ-ray spectrum, corrected for random coincidences; $P_{p\gamma}(E_0)$ is the conditional probability that a γ ray of energy E_0 is emitted in coincidence with the detected inelastically scattered proton. For the transitions of interest, the conditional probability $P_{p\gamma}(E_0)$ is unity.

Figure 28 shows individual points measured for the normalization function. The solid line shows the analytical interpolation used in our analysis,

$$\eta_\gamma(E_0)=4.11E_0^{-0.403}\times\exp[-0.0143(3.912+\ln E_0)^2-0.010(3.912+\ln E_0)^3]\ . \tag{A17}$$

3. Coincidence summing

For the average event analyzed in the present experiment, the individual NaI(Tl) modules in the backward hemisphere trigger with a coincidence probability of about $p=28\%$. This high probability is due to the rather large multiplicity of γ rays (and neutrons) emitted from highly excited target residues. Only a fraction, $1-p$, of recorded fragment γ rays will be corresponding to single γ-ray interactions for a given detector module; there is the probability p for the coincident interaction of a second γ ray or a neutron with the same detector module. This "coincidence summing" effect leads to considerable, multiplicity dependent line-shape distortions, see Fig. 5 of the main text. These line-shape distortions were evaluated by folding the fraction p of the original calibration function, Eq. (A1), with the normalized background function, $B_\gamma(E)$, obtained from an energy spectrum in the backward hemisphere of the spin spectrometer which reflects the pulse height distribution for neutrons and γ rays emitted from target residues. This latter spectrum was gated by the detection of a ^{9}Be fragment in a particle telescope to avoid introducing structures due to discrete γ rays emitted from the detected fragments. The corrected response function has the form

$$\varepsilon_\gamma^*(E,E_0,A_0,p)=A_0\{(1-p)\varepsilon_\gamma(E,E_0)+p\int_0^E dE'[\varepsilon_\gamma(E-E',E_0)B_\gamma(E')]\}, \tag{A18}$$

with

$$\int dE' B_\gamma(E')=1\ . \tag{A19}$$

where $\epsilon_\gamma(E,E_0)$ is the result of Eq. (A1) with $A_0=1$.

---

*Present address: Nuclear Chemistry Division, Lawrence Livermore National Laboratory, Livermore, CA 94550.

†Present address: Institut für Experimentalphysik, Universität Frankfurt, D-6000 Frankfurt, Federal Republic of Germany.

[1]Proceedings of the Symposium on Central Collisions and Fragmentation Processes, Denver, 1987 [Nucl. Phys. **A471**, 1 (1987)].

[2]W. G. Lynch, Annu. Rev. Nucl. Part. Sci. **37**, 493 (1987).

[3]E. K. Hyde, G. W. Butler, and A. M. Poskanzer, Phys. Rev. C **4**, 1759 (1971).

[4]A. M. Poskanzer, G. W. Butler, and E. K. Hyde, Phys. Rev. C **3**, 882 (1971).

[5]G. D. Westfall, R. G. Sextro, A. M. Poskanzer, A. M. Zebelman, G. W. Butler, and E. K. Hyde, Phys. Rev. C **17**, 1368 (1978).

[6]R. E. L. Green and R. G. Korteling, Phys. Rev. C **22**, 1594 (1980).

[7]R. W. Minich, S. Agarwal, A. Bujak, J. Chuang, J. E. Finn, L. J. Gutay, A. S. Hirsch, N. T. Porile, R. P. Scharenberg, B. C. Stringfellow, and F. Turkot, Phys. Lett. **118B**, 458 (1982).

[8]J. E. Finn, S. Agarwal, A. Bujak, J. Chuang, L. J. Gutay, A. S. Hirsch, R. W. Minich, N. T. Porile, R. P. Scharenberg, B. C. Stringfellow, and F. Turkot, Phys. Rev. Lett. **49**, 1321 (1982).

[9]A. S. Hirsch, A. Bujak, J. E. Finn, L. J. Gutay, R. W. Minich, N. T. Porile, R. P. Scharenberg, B. C. Stringfellow, and F. Turkot, Phys. Rev. C **29**, 508 (1984).

[10]A. I. Warwick, H. H. Wieman, H. H. Gutbrod, M. R. Maier, J. Péter, H. G. Ritter, H. Stelzer, F. Weik, M. Freedman, D. J. Henderson, S. B. Kaufman, E. P. Steinberg, and B. D. Wilkins, Phys. Rev. C **27**, 1083 (1983).

[11]K. A. Frankel and J. D. Stevenson, Phys. Rev. C **23**, 1511 (1981).

[12]B. Jakobsson, G. Jönsson, B. Lindkvist, and A. Oskarsson, Z. Phys. A **307**, 293 (1982).

[13]C. B. Chitwood, D. J. Fields, C. K. Gelbke, W. G. Lynch, A. D. Panagiotou, M. B. Tsang, H. Utsunomiya, and W. A. Friedman, Phys. Lett. **131B**, 289 (1983).

[14]L. G. Sobotka, M. L. Padgett, G. J. Wozniak, G. Guarino, A. J. Pacheo, L. G. Moretto, Y. Chan, R. G. Stokstad, I. Tserruya, and S. Wald, Phys. Rev. Lett. **51**, 2187 (1983).

[15]B. V. Jacak, G. D. Westfall, C. K. Gelbke, L. H. Harwood, W. G. Lynch, D. K. Scott, H. Stöcker, M. B. Tsang, and T. J. M. Symons, Phys. Rev. Lett. **51**, 1846 (1983).

[16]D. J. Fields, W. G. Lynch, C. B. Chitwood, C. K. Gelbke, M. B. Tsang, H. Utsunomiya, and J. Aichelin, Phys. Rev. C **30**, 1912 (1984).

[17]L. G. Sobotka, M. A. McMahan, R. J. McDonald, C. Signarbieux, G. J. Wozniak, M. L. Padgett, J. H. Gu, Z. H. Liu, Z. Q. Yao, and L. G. Moretto, Phys. Rev. Lett. **53**, 2004 (1984).

[18]R. Trockel, K. D. Hildenbranc, U. Lynen, W. F. J. Meuller, H. J. Rabe, H. Sann, H. Stelzer, R. Wada, N. Brummund, R. Glasow, K. H. Kampert, R. Santo, D. Pelte, J. Pochodzalla, and E. Eckert, Gessellschaft für Schwerionenforschung Report No. GSI-85-45, 1985.

[19]W. Mittig, A. Cunsolo, A. Foti, J. P. Wieleczko, F. Auger, B. Berthier, J. M. Pascaud, J. Québert, and E. Plagnol, Phys. Lett. **154B**, 259 (1985).

[20]R. Trockel, K. D. Hildenbrand, U. Lynen, W. F. J. Müller, H. J. Rabe, H. Sann, H. Stelzer, W. Trautmann, R. Wada, N. Brummund, R. Glasow, K. H. Kampert, R. Santo, D. Pelte, J. Pochodzalla, and E. Eckert, *Hadronic Matter in Collision,* edited by P. Carruthers and D. Strottman (World Scientific, Singapore, 1986), p. 291.

[21]D. J. Fields, W. G. Lynch, T. K. Nayak, M. B. Tsang, C. B. Chitwood, C. K. Gelbke, R. Morse, J. Wilczynski, T. C. Awes, R. L. Ferguson, F. Plasil, F. E. Obenshain, and G. R. Young, Phys. Rev. C **34**, 536 (1986).

[22]B. V. Jacak, G. D. Westfall, G. M. Crawley, D. Fox, C. K. Gelbke, L. H. Harwood, B. E. Hasselquist, W. G. Lynch, D. K. Scott, H. Stöcker, M. B. Tsang, G. Buchwald, and T. J. M. Symons, Phys. Rev. C **35**, 1751 (1987).

[23]K. Kwiatkowski, J. Bashkin, H. Karwowski, M. Fatyga, and V. E. Viola, Phys. Lett. B **171**, 41 (1986).

[24]M. Fatyga, K. Kwiatkowski, V. E. Viola, W. G. Wilson, M. B. Tsang, J. Pochodzalla, W. G. Lynch, C. K. Gelbke, D. J. Fields, C. B. Chitwood, Z. Chen, and T. Nayak, Phys. Rev. Lett. **58**, 2527 (1987).

[25]M. Fatyga, R. C. Byrd, K. Kwiatkowski, W. G. Wilson, L. W. Woo, V. E. Viola, Jr., H. J. Karwowski, J. Jastrzebski, and W. Skulski, Phys. Lett. B **185**, 321 (1987).

[26]R. Bougault, D. Horn, C. B. Chitwood, D. J. Fields, C. K. Gelbke, D. R. Klesch, W. G. Lynch, M. B. Tsang, and K. Kwiatkowski, Phys. Rev. C **36**, 830 (1987).

[27]T. C. Sangster, A. T. Bujak, D. D. Carmony, Y. H. Chung, L. J. Gutay, A. S. Hirsch, M. Mahi, G. L. Padrewski, N. T. Porile, R. P. Scharenberg, and B. C. Stringfellow, Phys. Lett. B **188**, 29 (1987).

[28]J. Pochodzalla, W. A. Friedman, C. K. Gelbke, W. G. Lynch, M. Maier, D. Ardouin, H. Delagrange, H. Doubre, C. Grégoire, A. Kyanowski, W. Mittig, A. Péghaire, J. Péter, F. Saint-Laurent, Y. P. Viyogi, B. Zwieglinski, G. Bizard, F. Lefèbvres, B. Tamain, J. Québert, Phys. Rev. Lett. **55**, 177 (1985).

[29]J. Pochodzalla, W. A. Friedman, C. K. Gelbke, W. G. Lynch, M. Maier, D. Ardouin, H. Delagrange, H. Doubre, C. Grégoire, A. Kyanowski, W. Mittig, A. Péghaire, J. Péter, F. Saint-Laurent, Y. P. Viyogi, B. Zwieglinski, G. Bizard, F. Lefèbvres, B. Tamain, J. Québert, Phys. Lett. **161B**, 275 (1985).

[30]C. B. Chitwood, C. K. Gelbke, J. Pochodzalla, Z. Chen, D. J. Fields, W. G. Lynch, R. Morse, M. B. Tsang, D. H. Boal, and J. C. Shillcock, Phys. Lett. B **172**, 27 (1986).

[31]H. M. Xu, D. J. Fields, W. G. Lynch, M. B. Tsang, C. K. Gelbke, M. R. Maier, D. J. Morrissey, J. Pochodzalla, D. G. Sarantites, L. G. Sobotka, M. L. Halbert, D. C. Hensley, D. Hahn, and H. Stöcker, Phys. Lett. B **182**, 155 (1986).

[32]J. Pochodzalla, C. K. Gelbke, W. G. Lynch, M. Maier, D. Ardouin, H. Delagrange, H. Doubre, C. Grégoire, A. Kyanowski, W. Mittig, A. Péghaire, J. Péter, F. Saint-Laurent, B. Zwieglinski, G. Bizard, F. Lefèbvres, B. Tamain, J. Québert, Y. P. Viyogi, W. A. Friedman, and D. H. Boal, Phys. Rev. C **35**, 1695 (1987).

[33]Z. Chen, C. K. Gelbke, J. Pochodzalla, C. B. Chitwood, D. J. Fields, W. G. Gong, W. G. Lynch, and M. B. Tsang, Nucl. Phys. **A473**, 564 (1987).

[34]Z. Chen, C. K. Gelbke, W. G. Gong, Y. D. Kim, W. G. Lynch, M. R. Maier, J. Pochodzalla, M. B. Tsang, F. Saint-Laurent, D. Ardouin, H. Delagrange, H. Doubre, J. Kasagi, A. Kyanowski, A. Péghaire, J. Péter, E. Rosato, G. Bizard, F. Lefèbvres, B. Tamain, J. Québert, and Y. P. Viyogi, Phys. Lett. B **199**, 171 (1987).

[35]Z. Chen, C. K. Gelbke, W. G. Gong, Y. D. Kim, W. G. Lynch, M. R. Maier, J. Pochodzalla, M. B. Tsang, F. Saint-Laurent, D. Ardouin, H. Delagrange, H. Doubre, J. Kasagi, A. Kyanowski, A. Péghaire, J. Péter, E. Rosato, G. Bizard, F. Lefèbvres, B. Tamain, J. Québert, and Y. P. Viyogi, Phys. Rev. C **36**, 2297 (1987).

[36]F. Saint-Laurent, A. Kyanowski, D. Ardouin, H. Delagrange, H. Doubre, C. Grégoire, W. Mittig, A. Péghaire, J. Péter, G. Bizard, F. Lefèbvres, B. Tamain, J. Québert, Y. P. Viyogi, J. Pochodzalla, C. K. Gelbke, W. Lynch, and M. Maier, Phys. Lett. B **202**, 190 (1988).

[37]David Boal, Phys. Rev. C **30**, 119 (1984).

[38]J. A. Lopez and P. J. Siemens, Nucl. Phys. **A431**, 728 (1984).

[39]K. Sneppen and L. Vinet, Nucl. Phys. **A480**, 342 (1988).

[40]D. H. Boal and J. N. Glosli, Phys. Rev. C **37**, 91 (1988).

[41]L. G. Moretto, Nucl. Phys. **A247**, 211 (1975).

[42]D. H. E. Gross, L. Satpathy, Meng Ta-chung, and M. Satpathy, Z. Phys. A **309**, 41 (1982).

[43]W. A. Friedman and W. G. Lynch, Phys. Rev. C **28**, 950

(1983).
[44]J. Randrup and S. E. Koonin, Nucl. Phys. **A356**, 223 (1981).
[45]G. Fài and J. Randrup, Nucl. Phys. **A281**, 557 (1982).
[46]J. P. Bondorf, S. I. A. Garpman, and J. Zimanyi, Nucl. Phys. **A296**, 320 (1978).
[47]S. Ben-Hao and D. H. E. Gross, Nucl. Phys. **A437**, 643 (1985).
[48]D. Hahn and H. Stöcker, Phys. Rev. C **35**, 1311 (1987).
[49]D. J. Fields, C. K. Gelbke, W. G. Lynch, and J. Pochodzalla, Phys. Lett. B **187**, 257 (1987).
[50]J. Gomez del Campo, J. L. Charvet, A. D'Onofrio, R. L. Auble, J. R. Beene, M. L. Halbert, and H. J. Kim, Phys. Rev. Lett. **61**, 290 (1988).
[51]T. J. Schlagel and V. R. Pandharipande, Phys. Rev. C **36**, 162 (1987).
[52]A. Vicentini, G. Jacucci, and V. R. Pandharipande, Phys. Rev. C **31**, 1783 (1985).
[53]R. J. Lenk and V. R. Pandharipande, Phys. Rev. C **34**, 177 (1986).
[54]W. Bauer *et al.*, Phys. Rev. Lett. **58**, 863 (1987).
[55]J. Aichelin, G. Peilert, A. Bohnet, A. Rosenhauer, H. Stöcker, and W. Greiner, Nucl. Phys. **A488**, 437 (1988), and references contained therein.
[56]D. H. Boal and J. N. Glosli, Phys. Rev. C **38**, 1870 (1988).
[57]P. J. Siemens and J. O. Rasmussen, Phys. Rev. Lett. **42**, 880 (1979).
[58]H. Stöcker, A. A. Ogloblin, and W. Greiner, Z. Phys. A **303**, 259 (1981).
[59]C. B. Chitwood, D. J. Fields, C. K. Gelbke, D. B. Klesch, W. G. Lynch, M. B. Tsang, T. C. Awes, R. L. Ferguson, F. E. Obenshain, F. Plasil, R. L. Robinson, and G. R. Young, Phys. Rev. C **34**, 858 (1986).
[60]D. J. Morrissey, W. Benenson, E. Kashy, B. Sherril, A. D. Panagiotou, R. A. Blue, R. M. Ronningen, J. van der Plicht, and H. Utsunomiya, Phys. Lett. **148B**, 423 (1984).
[61]D. J. Morrissey, W. Benenson, E. Kashy, C. Bloch, M. Lowe, R. A. Blue, R. M. Ronningen, B. Sherrill, H. Utsunomiya, and I. Kelson, Phys. Rev. C **32**, 877 (1985).
[62]D. J. Morrissey, C. Bloch, W. Benenson, E. Kashy, R. A. Blue, R. M. Ronningen, and R. Aryaeinejad, Phys. Rev. C **34**, 761 (1986).
[63]L. G. Sobotka, D. G. Sarantites, H. Puchta, F. A. Dilmanian, M. Jääskeläinen, M. L. Halbert, J. H. Barker, J. R. Beene, R. L. Ferguson, D. C. Hensley, and G. R. Young, Phys. Rev. C **34**, 917 (1986).
[64]C. Bloch, W. Benenson, A. I. Galonsky, E. Kashy, J. Heltsley, L. Heilbronn, M. Lowe, B. Remington, D. J. Morrissey, and J. Kasagi, Phys. Rev. C **36**, 203 (1987).
[65]A. Galonsky, G. Caskey, L. Hilbronn, B. Remington, H. Schelin, F. Deak, A. Kiss, Z. Seres, and J. Kasagi, Phys. Lett. B **197**, 511 (1987).
[66]M. Jääskeläinen, D. G. Sarantites, R. Woodward, F. A. Dilmanian, J. T. Hood, R. Jääskeläinen, D. C. Hensley, M. L. Halbert, and J. H. Barker, Nucl. Instrum. Methods **204**, 385 (1983).
[67]F. Ajzenberg-Selove, Nucl. Phys. **A392**, 1 (1983); **A413**, 1 (1984); **A433**, 1 (1985); **A449**, 1 (1986); **A460**, 1 (1986).
[68]B. A. Brown (private communication).
[69]Z. Chen and C. K. Gelbke, Phys. Rev. C **38**, 2630 (1988).
[70]A. Gilbert and A. G. W. Cameron, Can. J. Phys. **43**, 1446 (1965).
[71]R. G. Stokstad, in Proceedings of the Topical Conference on Heavy-Ion Collisions, Pikeville, 1977, edited by E. C. Halbert, J. A. Maruhn, V. Maruhn-Rezuani, and J. B. McGrory (unpublished).
[72]P. Marmier and E. Sheldon, *Physics of Nuclei and Particles* (Academic, New York, 1969), Vol. 1, p. 38.
[73]W. Hauser and H. Feshbach, Phys. Rev. **87**, 366 (1952).
[74]T. K. Nayak *et al.* (unpublished).
[75]T. K. Nayak, T. Murakami, W. G. Lynch, K. Swartz, D. J. Fields, C. K. Gelbke, Y. D. Kim, J. Pochodzalla, M. B. Tsang, H. M. Xu, F. Zhu, and K. Kwiatkowski, Phys. Rev. Lett. **62**, 1021 (1989).